Journal of Computational Physics **174,** 81–119 (2001)
doi:10.1006/jcph.2001.6896, available online at http://www.idealibrary.com on IDEAL®

Methods for the Accurate Computations of Hypersonic Flows

II. Shock-Aligned Grid Technique

Kyu Hong Kim, Chongam Kim, and Oh-Hyun Rho

Department of Aerospace Engineering, Seoul National University, Seoul 151-742, Korea

Received August 23, 1999; revised January 10, 2001

In order to eliminate or minimize the numerical error by shock waves due to grid distribution in multidimensional hypersonic flows, a new grid reconstruction scheme, the shock-aligned grid technique (SAGT), is proposed. The error due to shock waves in a non-shock-aligned grid system magnifies in proportion to the Mach number and propagates on the downstream side of the flow field to contaminate sensitive aerodynamic coefficients or flow quantities. SAGT, combined with the AUSMPW+ scheme proposed in Part I of the present work, not only provides an accurate solution but also reduces the grid dependency of a numerical scheme without a substantial increase in computational cost. In addition, SAGT is robust and flexible enough to deal with complex flow problems involving shock interaction and reflection and equilibrium and nonequilibrium effects. Extensive numerical tests from a hypersonic blunt body flow to hypersonic nonequilibrium flows validate the accuracy, efficiency, robustness, and convergence characteristics of SAGT.

---

1. INTRODUCTION

One of the distinct features in computing hypersonic aerodynamics is that it involves severe viscous dissipation in boundary layers and strong shock waves, which leads to the stiff gradient of flow properties or the reaction of air molecules. This imposes a high degree of accuracy, robustness, and efficiency in designing a numerical flux function or a time integration technique. For example, numerical dissipation has to be minimized to the degree that it does not produce unphysical numerical oscillations. At the same time, high frequency error around stiff gradient regions should be effectively damped out to avoid compromising solution accuracy or convergence characteristics.

For accurate computations of hypersonic flows, it is essential to examine primary factors that influence solution behavior critically. The present work focuses on the errors caused by

0021-9991/01 $35.00

a spatial discretization scheme and grid distribution. The first issue which was dealt with in Part I of the present work, proposed a AUSMPW+ scheme for determining the numerical flux function.

The treatment of the error by grid distribution is to be investigated in the present paper. One of the fundamental reasons for error near strong shocks in multidimensional flows is closely related to grid distribution since the position of shock discontinuity is usually not considered in generating a grid system. The error in the region of a shock wave is generally magnified in proportion to the Mach number or the distance between shock position and cell interface. It continuously propagates on the downstream side of a shock, causing solution inaccuracy and slow convergence. In addition, it may seriously affect sensitive aerodynamic coefficients or higher order flow quantities, such as surface heating rate, vorticity, and turbulence eddy viscosity [1]. This can be easily observed in cases of shock/shock interaction or flows involving physical oscillations. Thus the removal or minimization of the error due to a grid system is essential in computing hypersonic flow problems accurately.

Traditional methods to treat the error include mesh adaptation and a shock-fitting techniques. The mesh adaptation method is to redistribute or increase the number of grid points, based on a solution in a given grid system, around the region where a more accurate solution is required. This approach may reduce the error but does not eliminate it completely. Aside from the problem of the design of a robust error indicator, convergence characteristics and the time step limit from the CFL condition may get worse as grid size becomes smaller. In the shock-fitting technique, a shock wave is treated as a boundary, and a solution on the downstream side of a shock is determined using the Rankine–Hugoniot relation such that it is compatible with other parts of a solution. Since a shock does not spread even in multidimensional flows, the error caused by a shock can be avoided and a higher order scheme can be readily applied to obtain accurate results. However, this approach is not robust enough to be implemented in complex flow situations. For example, shock/shock interaction, shock reflection, complicated internal flow problems such as supersonic nozzle flows, and equilibrium and nonequilibrium flows are among the important test cases for which this approach cannot be applied.

Therefore, a fundamental way to eliminate or reduce the shock-induced error, within the framework of shock-capturing philosophy, is to generate a grid system that reflects shock position as accurately as possible. In other words, local grids need to be exactly aligned with shock waves in a systematic way. At the same time, the numerical scheme adopted should support the grid system in a way that allows it to capture normal or oblique shock waves over one cell interface in the shock-aligned grid system. Unless both conditions are satisfied, the error cannot be eliminated. The AUSMPW+ scheme, proposed in Part I of the present work, satisfies the requirements for shock capturing. In the present paper, a new grid reconstruction technique, the shock-aligned grid technique (SAGT), is proposed.

SAGT is a method to align cell interfaces of interest with shock waves *automatically*. In a general grid system, it is very difficult to exactly align a shock with cell interfaces by simply moving grid lines. It may be possible, only in a simple case, by a user's iterative efforts. For problems involving several shock waves, however, it is impossible to achieve a complete grid alignment with such brute-force attempts. The shock-fitting technique is also partially available since it cannot be applied to complicated flows involving shock/shock interaction or nonequilibrium effects. On the other hand, SAGT is robust and flexible enough to overcome those difficulties without a significant increase in computational cost. Using SAGT combined with AUSMPW+, accurate solutions can be obtained with minimal numerical errors.

The present paper is organized as follows. Following the introduction, a brief description on the governing equations and numerical discretizations is given in Section 2. In Section 3 the procedure of SAGT is explained in detail. Extensive test cases of SAGT with AUSMPW+ ranging from shock intersection and reflection to hypersonic equilibrium and nonequilibrium flows are presented in Section 4 to validate accuracy, efficiency, robustness, and convergence characteristics. Finally, conclusions based on the results of the previous sections are drawn.

2. GOVERNING EQUATIONS AND NUMERICAL DISCRETIZATIONS

The governing equations and spatial and temporal discretizations are the same as in the Part I of the present work. Thus, they are briefly introduced in this section.

The two-dimensional, axisymmetric Navier–Stokes equations in conservative form are used as

$$\frac{\partial \boldsymbol{Q}}{\partial t} + \frac{\partial \boldsymbol{E}}{\partial x} + \frac{\partial \boldsymbol{F}}{\partial y} = \left(\frac{\partial \boldsymbol{E}_v}{\partial x} + \frac{\partial \boldsymbol{F}_v}{\partial y} \right) + \boldsymbol{S}, \tag{1}$$

where $\boldsymbol{S}$ represents the source term due to thermochemical phenomena or axisymmetry. Three types of gases are considered according to the reaction effects of air molecules.

For a calorically perfect gas or equilibrium air molecules, the equation of state is given by

$$p = (\tilde{\gamma} - 1)\rho e = (\tilde{\gamma} - 1)\rho \left(e_t - \frac{1}{2}(u^2 + v^2) \right), \tag{2}$$

where $\tilde{\gamma}$ is 1.4 for a calorically perfect gas and is calculated by the curve-fitted data in Refs. [2, 3] for equilibrium air. For nonequilibrium air, the contribution of each molecular species is included to yield

$$p = \sum_s \rho_s \frac{R}{M_s} T, \tag{3}$$

where R is the universal gas constant (8.314 kJ/kg $\cdot$ mole $\cdot$ K) and M_s is the molecular weight of each species. All the effects of chemical species and vibrational energy are considered using the five-species (O_2, N_2, NO, O, N) chemical reaction model in the temperature range of $2500\,\mathrm{K} < T < 9000$ K [4, 5]. Then, the final flow and flux vectors are given by

$$\boldsymbol{Q} = \begin{pmatrix} \rho \\ \rho u \\ \rho v \\ \rho e_t \\ \rho_1 \\ \rho_2 \\ \rho_3 \\ \rho e_{vib,3} \\ \rho e_{vib,4} \\ \rho e_{vib,5} \end{pmatrix}, \qquad \boldsymbol{E} = \begin{pmatrix} \rho u \\ \rho u^2 + p \\ \rho u v \\ (\rho e_t + p) u \\ \rho_1 u \\ \rho_2 u \\ \rho_3 u \\ \rho e_{vib,3} u \\ \rho e_{vib,4} u \\ \rho e_{vib,5} u \end{pmatrix},$$

$$\boldsymbol{F} = \begin{pmatrix} \rho v \\ \rho u v \\ \rho v^2 + p \\ (\rho e_t + p) v \\ \rho_1 v \\ \rho_2 v \\ \rho_3 v \\ \rho e_{vib,3} v \\ \rho e_{vib,4} v \\ \rho e_{vib,5} v \end{pmatrix}, \qquad \boldsymbol{S} = \begin{pmatrix} 0 \\ 0 \\ 0 \\ 0 \\ \dot{w}_1 \\ \dot{w}_2 \\ \dot{w}_3 \\ \rho \dot{e}_{vib,3} + \dot{w}_3 e_{vib,3} \\ \rho \dot{e}_{vib,4} + \dot{w}_4 e_{vib,4} \\ \rho \dot{e}_{vib,5} + \dot{w}_5 e_{vib,5} \end{pmatrix}, \tag{4}$$

$$\boldsymbol{E}_v = \begin{pmatrix} 0 \\ \tau_{xx} \\ \tau_{xy} \\ e_v \\ \rho D_1 \frac{\partial c_1}{\partial x} \\ \rho D_2 \frac{\partial c_2}{\partial x} \\ \rho D_3 \frac{\partial c_3}{\partial x} \\ \rho e_{vib,3} D_3 \frac{\partial c_3}{\partial x} + \kappa_{vib,3} \frac{\partial T_{vib,3}}{\partial x} \\ \rho e_{vib,4} D_4 \frac{\partial c_4}{\partial x} + \kappa_{vib,4} \frac{\partial T_{vib,4}}{\partial x} \\ \rho e_{vib,5} D_5 \frac{\partial c_5}{\partial x} + \kappa_{vib,5} \frac{\partial T_{vib,5}}{\partial x} \end{pmatrix}, \qquad \boldsymbol{F}_v = \begin{pmatrix} 0 \\ \tau_{xy} \\ \tau_{yy} \\ f_v \\ \rho D_1 \frac{\partial c_1}{\partial y} \\ \rho D_2 \frac{\partial c_2}{\partial y} \\ \rho D_3 \frac{\partial c_3}{\partial y} \\ \rho e_{vib,3} D_3 \frac{\partial c_3}{\partial y} + \kappa_{vib,3} \frac{\partial T_{vib,3}}{\partial y} \\ \rho e_{vib,4} D_4 \frac{\partial c_4}{\partial y} + \kappa_{vib,4} \frac{\partial T_{vib,4}}{\partial y} \\ \rho e_{vib,5} D_5 \frac{\partial c_5}{\partial y} + \kappa_{vib,5} \frac{\partial T_{vib,5}}{\partial y} \end{pmatrix},$$

where $e_v = u\tau_{xx} + v\tau_{xy} - q_x$, $f_v = u\tau_{xy} + v\tau_{yy} - q_y$ and the subscripts (1–5) stand for chemical speices. The four-temperature model is mainly used to test the robustness of SAGT with AUSMPW+ unless it is mentioned specifically. For a calorically perfect gas or equilibrium air, all the species and vibrational energy equations are omitted and Eqs. (4) become

$$\begin{gathered} \boldsymbol{Q} = \begin{pmatrix} \rho \\ \rho u \\ \rho v \\ \rho e_t \end{pmatrix}, \quad \boldsymbol{E} = \begin{pmatrix} \rho u \\ \rho u^2 + p \\ \rho u v \\ (\rho e_t + p) u \end{pmatrix}, \quad \boldsymbol{F} = \begin{pmatrix} \rho v \\ \rho v u \\ \rho v^2 + p \\ (\rho e_t + p) v \end{pmatrix}, \\ \boldsymbol{E}_v = \begin{pmatrix} 0 \\ \tau_{xx} \\ \tau_{xy} \\ e_v \end{pmatrix}, \quad \boldsymbol{F}_v = \begin{pmatrix} 0 \\ \tau_{xy} \\ \tau_{yy} \\ f_v \end{pmatrix}. \end{gathered} \tag{5}$$

For a spatial discretization, AUSMPW+ is advocated as a baseline scheme because of its accuracy, robustness, computational efficiency, and convergence characteristics (see Part I of the present work for its validation). The property of AUSMPW+ that can capture a shock wave through one cell interface is prerequisite for the implementation of SAGT. The flux function of AUSMPW+ can be summarized as

$$\boldsymbol{F}_{1/2} = \bar{M}_L^{+} c_{1/2} \boldsymbol{\Phi}_L + \bar{M}_R^{-} c_{1/2} \boldsymbol{\Phi}_R + \left(\boldsymbol{P}_L^{+} \boldsymbol{P}_L + \boldsymbol{P}_R^{-} \boldsymbol{P}_R\right), \tag{6}$$

(i) for $m_{1/2} \geq 0$

$$\bar{M}_L^+ = M_L^+ + M_R^- \times ((1-w)\cdot(1+f_R) - f_L),$$
$$\bar{M}_R^- = M_R^- \times w(1+f_R),$$

(ii) for $m_{1/2} < 0$

$$\bar{M}_L^+ = M_L^+ \times w(1+f_L),$$
$$\bar{M}_R^- = M_R^- + M_L^+ \times ((1-w)\cdot(1+f_L) - f_R),$$

where the pressure-based weighting functions, w and $f_{L,R}$, are given by

$$w(p_L, p_R) = 1 - \min\left(\frac{p_L}{p_R}, \frac{p_R}{p_L}\right)^3, \tag{7}$$

$$f_{L,R} = \begin{cases} \left(\frac{p_{L,R}}{p_s} - 1\right)\min\left(1, \frac{\min(p_{1,L}, p_{1,R}, p_{2,L}, p_{2,R})}{\min(p_L, p_R)}\right)^2, & p_s \neq 0, \\ 0 & \text{elsewhere}, \end{cases} \tag{8}$$

with $p_s = P_L^+ p_L + P_R^- p_R$ and where (p_1, p_2) are pressures in the transversal direction with respect to a cell interface, which is explained in detail in Part I. The interpolation functions for the split Mach number and pressure of AUSMPW+ at a cell interface are given by

$$M^\pm = \begin{cases} \pm\frac{1}{4}(M \pm 1)^2, & |M| \leq 1 \\ \frac{1}{2}(M \pm |M|), & |M| > 1, \end{cases} \tag{9}$$

$$P^\pm|_\alpha = \begin{cases} \frac{1}{4}(M \pm 1)^2(2 \mp M) \pm \alpha M(M^2-1)^2, & |M| \leq 1, \\ \frac{1}{2}(1 \pm \operatorname{sign}(M)), & |M| > 1, \end{cases} \tag{10}$$

where $0 \leq \alpha \leq 3/16$.

The Mach number on each cell side is defined as

$$M_{L,R} = \frac{U_{L,R}}{c_{1/2}}, \tag{11}$$

where $c_{1/2}$ is the speed of sound at a cell interface. For SAGT, $c_{1/2}$ should be formulated such that it can support the capturing of a shock through one cell interface. In order to satisfy this, the speed of sound in AUSMPW+ is designed as follows:

$$\begin{aligned} &\text{(i)} \quad \frac{1}{2}(U_L + U_R) > 0: \quad c_{1/2} = c_s^2 \big/ \max(|U_L|, c_s), \\ &\text{(ii)} \quad \frac{1}{2}(U_L + U_R) < 0: \quad c_{1/2} = c_s^2 \big/ \max(|U_R|, c_s). \end{aligned} \tag{12}$$

The speed of sound, c_s, is formulated from the conservation laws normal to an oblique shock as

$$c_s = \left(2H_{normal}\frac{(\tilde{\gamma}_L - 1)/\tilde{\gamma}_L\rho_L - (\tilde{\gamma}_R - 1)/\tilde{\gamma}_R\rho_R}{(\tilde{\gamma}_R - 1)/\tilde{\gamma}_R\rho_L - (\tilde{\gamma}_L + 1)/\tilde{\gamma}_L\rho_R}\right)^{0.5}, \tag{13}$$

where $H_{normal} = 0.5 \times (H_{total,L} - 0.5 \times V_L^2 + H_{total,R} - 0.5 \times V_R^2)$ and the subscripts (L, R) stand for the left and right side quantities across a cell interface.

For a higher order extension, a MUSCL (monotone upstream-centered scheme for conservation laws) approach based on primitive variables is adopted.

As a temporal integration, the governing equations are discretized by the backward Euler method, and the Jacobian matrices are inverted approximately by an AF-ADI or LU-SGS scheme. The AF-ADI scheme is used for a calorically perfect gas and an equilibrium gas. In a nonequilibrium gas, the LU-SGS scheme is adopted for the efficient calculation of the flux Jacobian and matrix inversion.

3. SHOCK-ALIGNED GRID TECHNIQUE

It is important to eliminate or minimize the error due to a grid system for accurate computations of hypersonic flows because the error or numerical instability generally increases in proportion to the Mach number. This can be easily seen in non-shock-aligned grids which do not take into account positions of physical discontinuities. Even with most accurate schemes that can capture a shock discontinuity through one cell interface in a shock-aligned grid system, such as Roe's FDS or some AUSM-type schemes, large errors behind shocks or oscillatory behavior can be easily observed when they are applied to non-shock-aligned grids. Moreover, negative properties may be frequently obtained in severe test cases. As a way to improve these situations, a grid system should reflect positions of physical shock discontinuities as exactly as possible. Through a shock-aligned grid system, a shock wave can be captured with minimal numerical errors.

The SAGT is a method of grid reconstruction that considers positions of physical discontinuities obtained from an initial converged solution in the original non-shock-aligned grids. The topology of the initial structured grids is changed locally in a way that cell interfaces are aligned with shock discontinuities *automatically*. Under the assumption that a numerical scheme has the capability of capturing a shock discontinuity without numerical errors and that an initial solution is sufficiently converged, SAGT determines the shock position very accurately and minimizes the error caused by inaccurate grid distribution in the region of shock waves. This advantage is more conspicuous in hypersonic flow computations since the error across a shock wave is quite significant. In the case of a blunt body problem where only one bow shock exists, it may be possible to align local cell interfaces with a shock by a user's experience, though complete alignment is difficult. However, in more complicated situations such as the generation or intersection of several shocks, it is impossible to construct *a priori* a shock-aligned grid system. By implementing SAGT systematically, however, a shock-aligned grid system can be easily generated from initial grids and an accurate solution with minimal numerical errors can be obtained.

3.1. Requirements for SAGT

In order for SAGT to be readily applicable, a numerical scheme adopted should satisfy the following two conditions.

(i) An oblique shock as well as a normal shock should be captured with only *one* cell interface if it is aligned with cell interfaces.

(ii) A numerical scheme should maintain a high level of robustness in calculating the shock region.

The first condition is needed because SAGT assumes that shock discontinuities are captured through only one cell interface after successful implementation. Shock capturing with one cell interface plays a key role as the barometer for checking the convergence of shock position. The second condition is necessary for the stable convergence of shock position. Unless a scheme satisfies the second condition, negative properties can be easily produced owing to temporary numerical error introduced by the change of grid topology in the process of aligning the shock with the grid.

There are several schemes to satisfy the first condition, including AUSM+, Roe's FDS, and AUSMPW+. AUSM+ with the speed of sound in Eqs. (12) and (13) is able to capture shocks without numerical error even for reacting gas flows. Moreover, it can overcome numerical instability due to the abrupt change of grid topology. However, it shows oscillatory phenomena which take much more computational time in the convergence of shock position. Roe's FDS, which has a numerical dissipation matrix that becomes zero at the sonic point, also captures shocks without numerical dissipation. Unfortunately, it does not survive the instability. According to the authors' experience, AUSMPW+ is the most appropriate scheme for the implementation of SAGT. Like AUSM+, AUSMPW+ captures shocks without numerical error and it is robust enough to overcome the instability caused by shocks. In addition, it does not show any oscillatory behavior, which leads to the fast convergence of shock position.

3.2. Procedure of SAGT

Figure 1 shows the brief procedure of SAGT. In a non-shock-aligned grid system, a shock is usually captured over the grid points with different grid index numbers. As shown in Fig. 1d, a numerical shock is located at cell interfaces, and large error is introduced at the grid points where grid indexes change. The error in this region is usually more than one order of magnitude larger compared to that in other regions, and it increases in proportion to the Mach number. Moreover, it propagates on the downstream side and compromises the accuracy of a computed solution, as indicated in Fig. 1d. With a lower Mach number, it does not cause a serious problem. In hypersonic flows, however, the error is large enough to contaminate the downstream flow field behind shocks. The main purpose of SAGT is to increase solution accuracy by aligning local grids with shocks. From Fig. 1c it can be easily seen that SAGT yields much more accurate results.

The SAGT is composed of the following three main steps:

Step 1. Calculation of Shock Position—Calculate shock position from an initial converged solution in a given grid system.

Step 2. Reconstruction of Grid System—Change the topology of local grids such that local cell interfaces are aligned with the calculated shock position in Step 1.

Step 3. Convergence of Solution—Obtain a converged solution iteratively in a shock-aligned grid system.

The detailed flowchart is given in Fig. 2.

3.2.1. *Step 1: Calculation of Shock Position*

a. Search for the region of stiff pressure gradient. The region of local maximum pressure is determined for the detection of shock position in Step 1.c. In a simple case of a single shock, we first search a cell interface index in the j-direction (normal to the wall) that has the

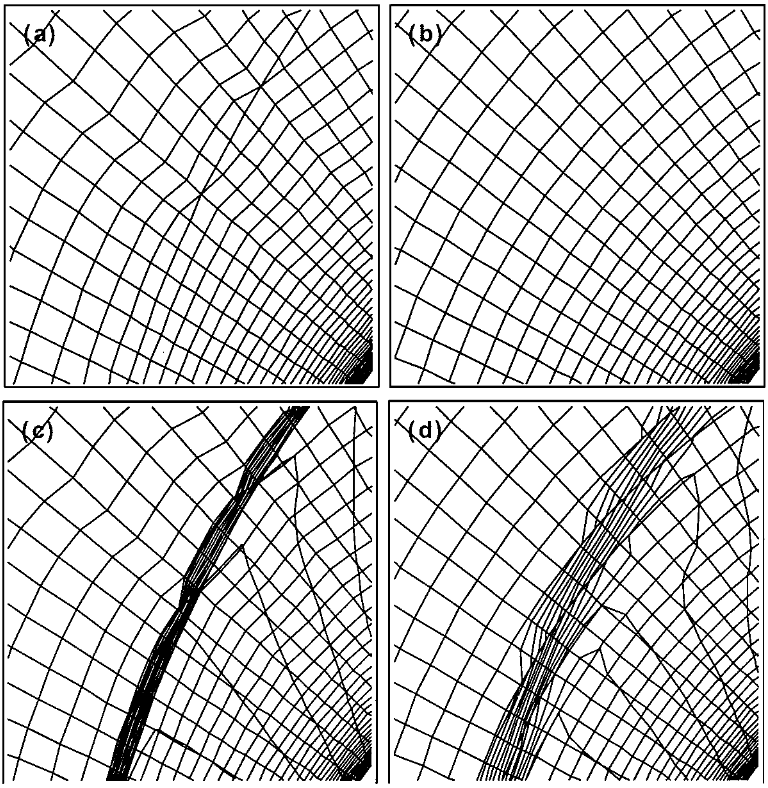

FIG. 1. Comparison of shock-aligned grids with non-shock-aligned grids.

local maximum pressure difference, $|p_{i,j+1} - p_{i,j}|$, with the i-index (parallel to the wall) fixed. And, a set of indexes $(i,\ j)$ is tagged as temporal shock front indexes (TSFI). TSFI for several shocks can be obtained similarly. With a given i-index, j-indexes are tagged if the pressure difference is greater than a threshold value, which is determined by some fraction of maximum pressure difference in the computational domain. The j-indexes are then rearranged according to the magnitude of the pressure differences. For example, it is assumed that there are five temporal shock front indexes for a given i-index:

$$\begin{gathered} \mathit{TSFI}(1,i) = 7, \qquad \mathit{TSFI}(2,i) = 12, \qquad \mathit{TSFI}(3,i) = 8, \\ \mathit{TSFI}(4,i) = 13, \qquad \mathit{TSFI}(5,i) = 4. \end{gathered} \tag{14}$$

If the difference of the *TSFI*, $|\mathit{TSFI}(n,i) - \mathit{TSFI}(n',i)|$, is equal to one, both indexes are considered to represent the same shock. Otherwise, they are assumed to indicate different shocks. In this case, the first and the third, and the second and the fourth, indexes represent the same shock, respectively. As a result, the number of shocks is three and the TSFI are

$$\mathit{TSFI}(1,i) = 12, \qquad \mathit{TSFI}(2,i) = 7, \qquad \mathit{TSFI}(3,i) = 4, \tag{15}$$

for a given i-index. By applying the same procedure for all i-indexes, the TSFI are completely determined.

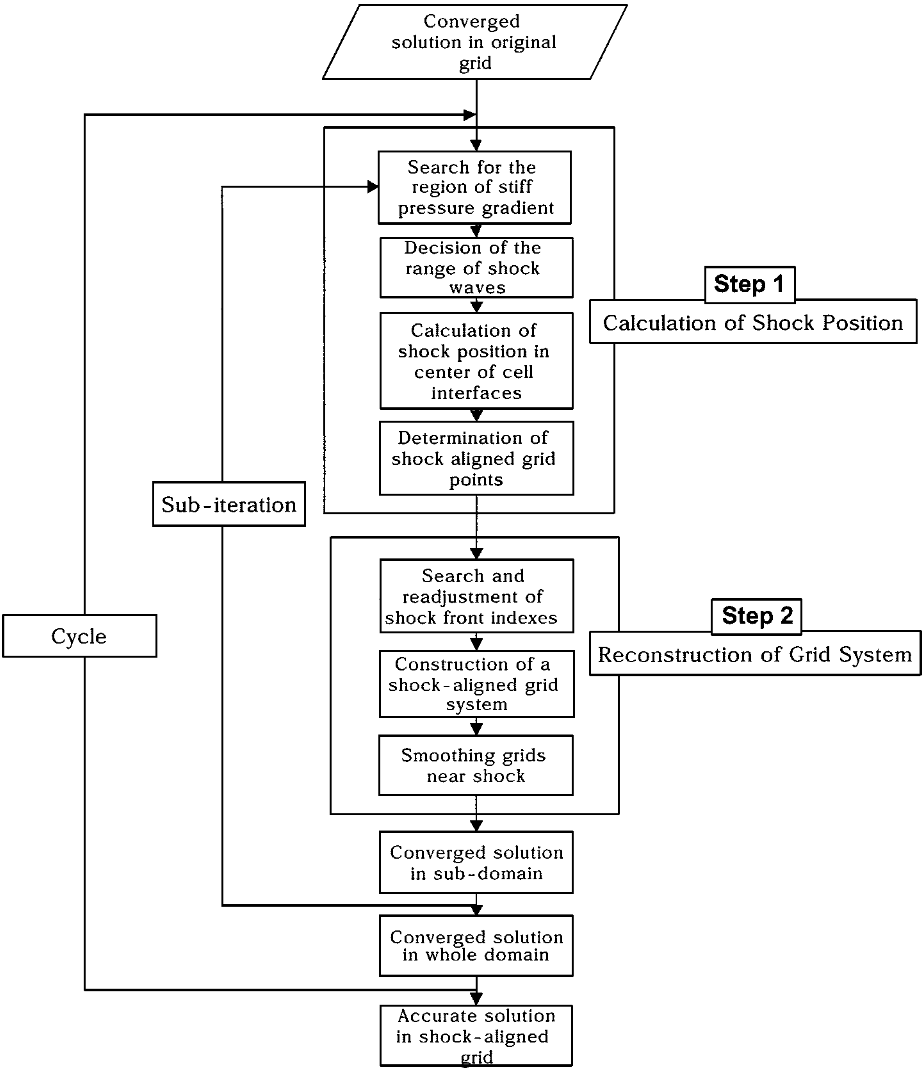

FIG. 2. Flowchart of shock-aligned grid technique.

Figure 3a shows the TSFI with dash-dot lines as

$$\begin{gathered} TSFI(1,1) = 2, \qquad TSFI(1,2) = 2, \qquad TSFI(1,3) = 3, \\ TSFI(1,4) = 3, \qquad TSFI(1,5) = 4. \end{gathered} \tag{16}$$

It can be seen that the value of the j-index is changed at $i = 3$ and 5, where a lot of error is inevitably induced. The error should be carefully treated to obtain accurate results since the amount is significant, which will be mentioned in detail in Step 2.c.

b. Decision of the range of shock waves. A shock is commonly captured through several cell interfaces due to numerical dissipation in a non-shock-aligned grid system. Thus the range of a shock can be assumed from $j - m - 1$ to $j + n$ for a given i-index as shown in Fig. 4, where j is the temporal shock front index determined in Step 1.a. Then, the range of a shock is specified by comparing pressure differences between the two neighboring points.

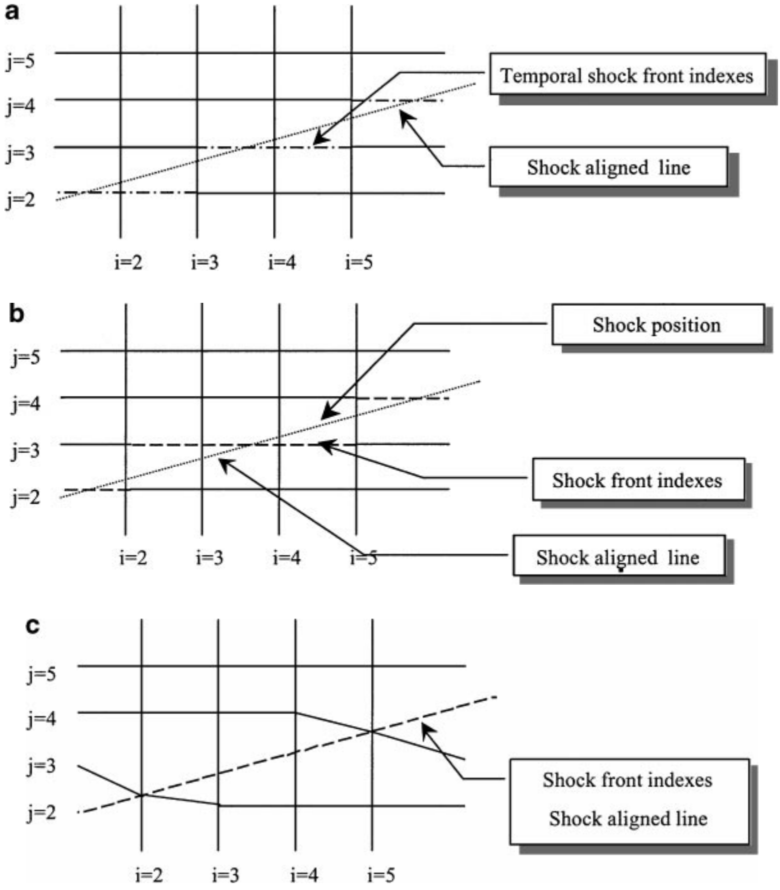

FIG. 3. (a) Search of temporal shock front indexes and interpolation of shock-aligned grid points (Step 1). (b) Search of shock front indexes, which is a set of j-indexes nearest to calculated shock positions (Step 2). (c) Movement of two end points of shock front indexes onto shock-aligned grid points (Step 2).

When $p_j > p_{j-1}$,

$$\frac{p_{j+n+1} - p_{j+n}}{p_j - p_{j-1}} > dp_{\max}, \tag{17}$$

$$\frac{p_{j-m-1} - p_{j-m-2}}{p_j - p_{j-1}} > dp_{\max}, \tag{18}$$

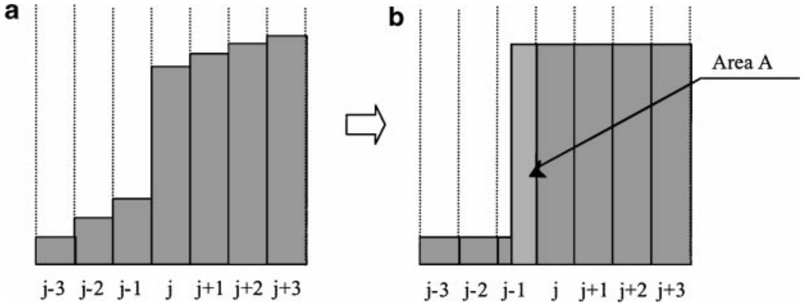

FIG. 4. Calculation of shock position. (a) Before shock detection; (b) after shock detection.

where $dp_{\max}$ is the maximum allowable pressure difference. In a coarse grid system, it is commonly 0.1, and in a dense grid system, it is 0.01. As it decreases, more accurate results can be obtained though shock position converges slowly. The values of m and n for each index i are determined by applying Eqs. (17) and (18) to the whole range of j-index. For an oblique shock, m or n is usually four or five; m or n is one or two for a normal shock. After the complete implementation of SAGT, m and n become zero, meaning that a shock is captured through one cell interface. In case of several shocks, care should be taken so that the range of one shock does not include the TSFI of the other shocks. Otherwise, significant error is induced in calculating shock position in Step 1.c, and the solution does not converge. Thus the nth shock range of the index i should satisfy the following constraint:

$$j - m - 1 \geq \mathit{TSFI}(n-1, i) + 1, \tag{19}$$

$$j + n \geq \mathit{TSFI}(n+1, i). \tag{20}$$

c. Calculation of shock position. Assuming that a shock is eventually captured through one cell interface as shown in Fig. 4b, shock position is estimated by

$$\sum_k p_k \Delta x_k|_{(a)} = \sum_k p_k \Delta x_k|_{(b)}, \tag{21}$$

where Δx_k is the distance between the kth and the $(k+1)$th cell interface. If area A is $\alpha_i \Delta x_j$, α is obtained from Eq. (21). When $p_j > p_{j-1}$,

$$\alpha_i = \frac{\sum_{k=j-m-1}^{k=j+n} p_k \Delta x_k\big|_{(a)} - p_{fs} \sum_{k=j-m-1}^{k=j-1} \Delta x_k\big|_{(b)} - p_{bs} \sum_{k=j}^{k=j+n} \Delta x_k\big|_{(b)}}{(p_{bs} - p_{fs})\Delta x_j}, \tag{22}$$

for $1 < i < i_{\max}$. p_{fs} is the pressure in front of a shock and p_{bs} the pressure behind a shock. Thus the estimated shock position is the geometric center of the shock region. The value of $\|\alpha\| = (\sum_i \alpha_i^2)^{1/2}$ is the barometer to check the convergence of shock position. If $\|\alpha\|$ becomes zero, the shock position is completely converged.

In the stagnation region of a blunt body, there are gradients of flow properties caused by physical compression processes even after a shock. Thus the range of a shock needs to be carefully determined so that it does not interfere with the region of physical compression. This is achieved by modifying the pressure behind a shock using dp_{buffer} and $dp_{\min}$, where

$$\begin{aligned} dp_{\mathit{buffer}} &= \frac{p_{j+n} - p_{bs}}{p_{bs} - p_{fs}}, \qquad \frac{p_{j+n+2} - p_{j+n+1}}{p_{j+n+1} - p_{j+n}} \geq 0, \\ dp_{\mathit{buffer}} &= \frac{p_{j+n+1} - p_{bs}}{p_{bs} - p_{fs}}, \qquad \frac{p_{j+n+2} - p_{j+n+1}}{p_{j+n+1} - p_{j+n}} < 0, \end{aligned} \tag{23}$$

and where p_{j+n+1} is the pressure in the cell next to the shock range. Then, p_{bs} is modified as

$$p_{bs} = \begin{cases} \frac{(p_{j+n} + dp_{buffer} \cdot p_{fs})}{1 + dp_{buffer}} & n > 0, \frac{p_{j+n+2} - p_{j+n+1}}{p_{j+n+1} - p_{j+n}} \geq 0, \\ \frac{(p_{j+n+1} + dp_{buffer} \cdot p_{fs})}{1 + dp_{buffer}} & n > 0, \frac{p_{j+n+2} - p_{j+n+1}}{p_{j+n+1} - p_{j+n}} < 0, \\ \frac{(p_{j+1} + dp_{\min} \cdot p_{j-1})}{1 + dp_{\min}}, & n = 0, \left| \frac{p_{j+1} - p_j}{p_j - p_{j-1}} \right| < dp_{\min}, \\ p_j, & \text{elsewhere}, \end{cases} \tag{24}$$

$$p_{fs} = p_{j-m-1}, \tag{25}$$

where $dp_{\min} \leq dp_{buffer} \leq dp_{\max} \cdot dp_{\min}$ is a minimum threshold value for the pressure difference. dp_{buffer} and $dp_{\min}$ give a buffer zone to accelerate the convergence of shock position. In a coarse grid system, $dp_{\min}$ is commonly 0.02, whereas in a dense grid system it is 0.005. dp_{buffer} is given as

$$dp_{buffer} = 0.75 \cdot dp_{\min} + 0.25 \cdot dp_{\max}. \tag{26}$$

When the flow behind the shock range is compressed again, that is,

$$\frac{p_{j+n+2} - p_{j+n+1}}{p_{j+n+1} - p_{j+n}} > 0,$$

dp_{buffer} and $dp_{\min}$ exclude the possibility that p_{bs} is overestimated. It should be noted that pressure behind a shock is temporary until shock position is completely converged. Once it is converged, however, it is equal to the pressure at j.

d. Determination of shock-aligned grid points. The purpose of this step is to obtain shock-aligned grid points based on the calculated shock position. From the result of Step 1.c, the location of a shock-aligned grid point is interpolated from center points of neighboring shock positions (see Fig. 3a and 3b). In this step, the position of interpolated shock-aligned grid points should be completely consistent with the constraint of Eq. (21). Otherwise, the center point of the shock position after interpolation, which is now the center point of the two shock-aligned grid points, is different from the center point before interpolation. As a result, significant error can be incurred since a shock will be eventually placed along shock-aligned grid points that are determined by interpolation.

Special care needs to be taken when there is a curvature of a shock, such as with a bow shock, as shown in Fig. 5a. $Sp_{c,i}$ indicates the center of shock position for a given i-index. In this case, the slope of $(Sp_{c,i+1}, Sp_{c,i})$ is different from that of $(Sp_{c,i}, Sp_{c,i-1})$. If the shock-aligned grid points (Sp_{i+1}, Sp_i) are determined by the linear interpolation of $(Sp_{c,i+1}, Sp_{c,i}, Sp_{c,i-1})$, it does not satisfy the constraint of Eq. (21), as shown in Fig. 5b. Since the shock will be eventually located along the grid points (Sp_{i+1}, Sp_i), it leads to a substantial amount of error. Thus the location of the interpolated grid points should be modified to satisfy Eq. (21) as follows. First, they are assumed to be determined by an arbitrary interpolation method as shown in Fig. 5a. Then (Sp_{i+1}, Sp_i) are moved to the final interpolated grid points (Sp'_i, Sp'_{i+1}), as shown in Fig. 5b, to compensate for the difference between the center points, $Sp_{c,i}$ and A:

$$p_i \cdot (Sp_{c,i} - B) = p_i \left(\frac{Sp'_{i+1} + Sp'_i}{2} - B \right). \tag{27}$$

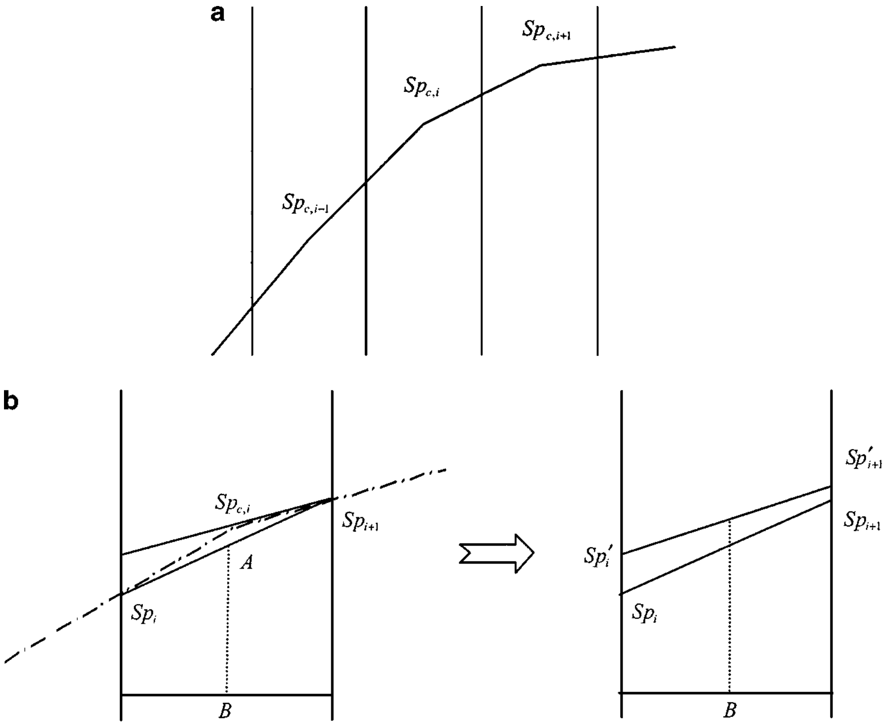

FIG. 5. (a) Effect of shock curvature. (b) Interpolation of shock-aligned grid points.

Then

$$Sp_{c,i} = \frac{Sp'_{i+1} + Sp'_i}{2}. \tag{28}$$

Thus we have

$$Sp'_{i-1} + 2Sp'_i + Sp'_{i+1} = 2(Sp_{c,i-1} + Sp_{c,i}), \tag{29}$$

for $2 < i < i_{\max} - 1$. Equation (29) forms a tri-diagonal matrix that can be solved implicitly. Unfortunately, if the grid topology changes abruptly, that is, $\|\alpha\|$ has a large value, the accurate solution of Eq. (29) may not be obtained. Thus the diagonal dominance is enforced to Eq. (29) by adding the linear interpolation equation:

$$Sp'_{i-1} + \left(2 + \|\alpha\|^{0.5}\right) Sp'_i + Sp'_{i+1} = \left(2 + \frac{\|\alpha\|^{0.5}}{2}\right)(Sp_{c,i-1} + Sp_{c,i}). \tag{30}$$

As a result, Eq. (21) is satisfied since $\|\alpha\|$ becomes zero after the complete convergence of shock position. The condition for the boundary grid points is

$$Sp'_1 = 1.5Sp_1 - 0.5Sp_2, \quad Sp'_{i\ \max} = 1.5Sp_{i\ \max} - 0.5Sp_{i\ \max-1}. \tag{31}$$

After finishing Step 1, shock-aligned grid points and shock position are completely determined.

3.2.2. *Step 2: Reconstruction of Grid System*

a. Search and determination of shock front indexes. Shock front indexes are defined as a set of indexes for which cell interfaces should be aligned with shock discontinuities. They consist of the cell interface indexes nearest the calculated shock position that are obtained in the previous Step 1 (see Fig. 3b). It should be noted that the TSFI in Step 1 may not be the same as the shock front indexes if α_i of Eq. (22) is greater than 0.5. After SAGT is successfully applied, the line formed by shock front cell interfaces directly represents a shock discontinuity. Shock front indexes contain the information

$$SFI(n, i) = j, \tag{32}$$

where n indicates the nth shock discontinuity. Equation (32) means that the nth shock discontinuity is located on the cell interface $(i,\ j)$. In the case of several shocks, such as a shock intersection problem, n is more than two for a given i-index. Figure 3b shows the shock front indexes with dash-dash lines, and these are seen to be different from the TSFI.

b. Readjustment of shock front indexes. In order to obtain good quality grids, it is required that neighboring shock front cell interfaces should not be separated more than one grid size, meaning that

$$|SFI(n, i+1) - SFI(n, i)| \leq 1. \tag{33}$$

In cells of high aspect ratio, however, Eq. (33) is violated. Then, unlike the usual case of Fig. 1a, more than three grid points can be merged into one shock-aligned grid point. As a result, grid quality deteriorates and convergence characteristics becomes poor. To prevent this, the shock front indexes are readjusted to satisfy Eq. (33). For example, if shock front indexes are

$$SFI(1, i-2) = 2, \quad SFI(1, i-1) = 2, \quad SFI(1, i) = 4,$$
$$SFI(1, i+1) = 5, \quad SFI(1, i+2) = 6,$$

$SFI(1, i-1)$ and $SFI(1, i)$ are rearranged as

$$SFI(1, i-2) = 2, \quad SFI(1, i-1) = 3, \quad SFI(1, i) = 4,$$
$$SFI(1, i+1) = 5, \quad SFI(1, i+2) = 6.$$

Since Step 1 and Step 2 are mutually independent, good quality grids can be obtained as long as the shock front indexes satisfy the condition of Eq. (33). It should be observed that the implementation of SAGT does not always bring the change of grid connectivity. If you make $SFI(n, i)$ constant for all i-indexes, high quality shock-aligned grids can be obtained without the change of grid topology, as shown in Fig. 14. However, in the general case involving shock intersection or reflection, the change of shock front indexes is inevitable.

c. Construction of a shock-aligned grid system. In this step, a shock-aligned grid system is made using shock-aligned grid points calculated in Step 1 and shock front indexes obtained in Steps 2.a and 2.b. This is accomplished by simply connecting two end points of a shock front index to shock-aligned grid points to form shock-aligned line:

$$\begin{aligned} x(i, SFI(n,i)) &= Sp'_{i,x}, \quad y(i, SFI(n,i)) = Sp'_{i,y} \\ x(i-1, SFI(n,i)) &= Sp'_{i-1,x}, \quad y(i-1, SFI(n,i)) = Sp'_{i-1,y}. \end{aligned} \tag{34}$$

As a result, grid connectivity is locally changed. Figure 3c shows the shock-aligned grid system after this step. In an initial structured grid system, a substantial amount of error is induced from the shock discontinuity region where the j-index of the shock front indexes changes as shown in Fig. 3b. The error is removed or minimized by the shock-aligned grid system as in Fig. 3c.

d. Smoothing grid points. After constructing shock-aligned grid points, smoothing near the shock region has to be carried out to improve grid quality, which is needed for the fast convergence and accuracy of a numerical solution. For the shock front index j, grid points within $j-5$ and $j+5$ are smoothed. In the smoothing process, the location of shock-aligned grid points, that is, shock position, must not be changed to maintain the property of Eq. (21).

3.2.3. *Step 3: Convergence of Solution*

In Step 3, an accurate solution is obtained by applying shock-aligned grids in a recursive manner.

a. Sub-iteration. A converged shock position and a final shock-aligned grid system are obtained based on the solution of an initial grid system. In the region where the location of the grid points is altered, a new accurate solution is obtained by simple explicit time integration to remove the error due to the change of grid topology and grid smoothing. The calculation of shock position and grid reconstruction process are repeated until $\|\alpha\|$ becomes zero, which means that shock position is converged. Although the error in this region is eliminated through sub-iteration, it does not necessarily mean that the whole computational domain is free from the error. Thus SAGT is applied repetitively.

b. Cycle. Since an initial converged solution has in general numerical error as shown in Fig. 1d, which is especially noticeable with a low quality grid, a shock-aligned grid solution is not free from the error. Thus, the whole SAGT process needs to be applied more than once (see Fig. 6). However, most of the error is usually eliminated in the first cycle and the difference in shock position is negligible. According to numerous computations, two cycles turn out to be sufficient to obtain an accurate converged solution. Any additional cycles do not provide a noticeable improvement in accuracy.

3.2.4. *Treatment of Shock Intersection or Reflection*

SAGT is robust enough to be applied successfully in problems involving shock intersection or reflection. A specific process needs to be added in Step 1.d to solve such problems accurately. In SAGT, the intersection or reflection of shocks is detected by comparing temporal shock front indexes. With regard to this, the following procedure should be added in Step 1.d:

a. Determine the shock intersection or reflection region.
b. Interpolate the shock-aligned grid points in shock intersection or reflection region.

Figure 7 shows the process of SAGT for a shock reflection problem.

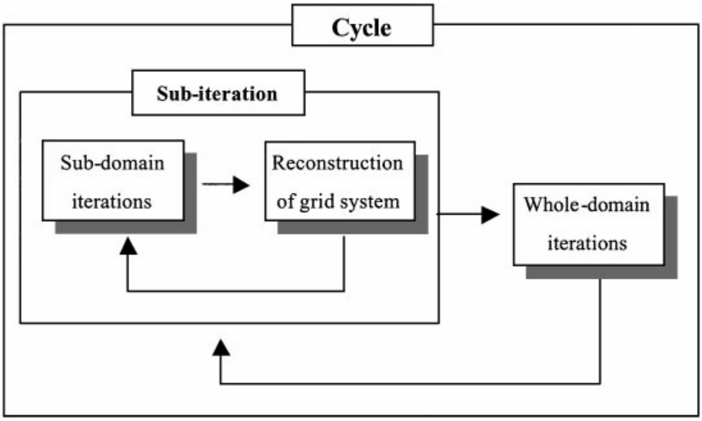

FIG. 6. Procedure of sub-iteration and cycle.

a. Determination of shock intersection or reflection regions. The shock intersection or reflection region is commonly spread over one to five cells. Thus the region is determined by checking the difference between temporal shock front indexes. If the difference is less than three for a given i-index, the region is tagged as the area of shock intersection or reflection.

For the shock intersection problem,

$$TSFI\,(n, i) - TSFI(n-1, i) \leq 3. \tag{35}$$

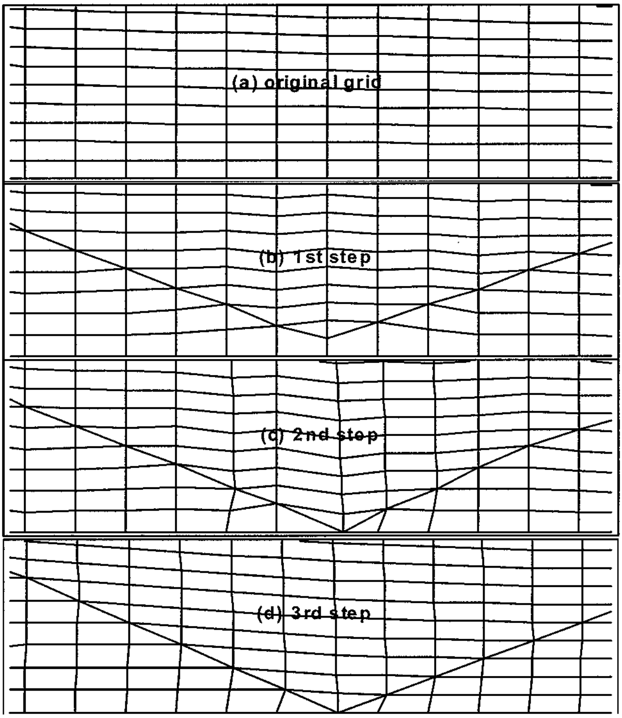

FIG. 7. SAGT process for the problem of shock reflection.

For the shock reflection problem,

$$|TSFI(n, i) - j_{wall}| \leq 3. \tag{36}$$

b. Interpolation of shock-aligned grid points in shock intersection or reflection region. Owing to insufficient cells in this region, shock-aligned grid points in Step 1.d may be calculated inaccurately. Thus the following modification is necessary.

For the index i, the region of interest is taken as $i - k$ to $i + k$ with $1 \leq k \leq 2$. Then, the intersection or reflection point is recalculated by extrapolation using neighboring shock positions of the index i. It is the intersection point of two lines passing through the points $Sp_{c,i-k-1}$ and $Sp_{c,i-k-2}$ for the nth and $n + 1$th shock position, respectively. Other shock-aligned grid points within the region of interest are interpolated using the newly determined point and neighboring shock positions of $Sp_{c,i-k-1}$ and $Sp_{c,i-k+1}$.

In addition, there are minor constraints for the fast convergence of shock position. In Step 2.b where shock front indexes are readjusted to satisfy Eq. (33), the shock front index of intersection or reflection must not change. Otherwise, the shock position may be converged very slowly. Also, in Step 3.a, it is desirable to divide the computational domain with respect to the intersection point and to apply the sub-iteration step separately, i.e., to the upstream shock region first and then to the downstream shock region. This removes the downstream propagation of upstream shock error and contributes to the fast convergence of shock position in the whole domain.

3.3. Quality of Grid System by SAGT

The purpose of SAGT is to *automatically* reconstruct a grid system that supports the capturing of shock discontinuities with little numerical error. SAGT is independent of a numerical scheme as long as it is able to capture a shock with only one cell interface in a shock-aligned grid system, such as AUSMPW+. In addition, SAGT is independent of the accuracy, robustness, or efficiency of a solver since it just provides a grid system.

The quality of a grid system by SAGT can be controlled by the threshold value in Eqs. (17), (18), and (24). In the present computations, the maximum pressure difference of 5% ($dp_{\max} = 0.05$) with respect to the pressure jump across a shock is allowed. More accurate results can be obtained by reducing the threshold value at the expense of convergence behavior. Figure 8 shows a typical spatial error distribution computed with the original grids and shock-aligned grids. The error is defined as

$$\text{error} = F_{1/2\,,mass} - \frac{1}{2}(\rho_L U_L + \rho_R U_R), \tag{37}$$

where $F_{1/2\,,mass}$ is the mass flux at a cell interface using the AUSMPW+ scheme, and U is the velocity component normal to a cell interface. As shown in Figs. 8 and 9, the error in the region of a shock is reduced more than one order of magnitude. Although the result of shock-aligned grids shows some error at the kinked grid points, it does not compromise solution accuracy as shown in Section 4.1. Moreover, the error may be reduced further with a smaller dp_{max}.

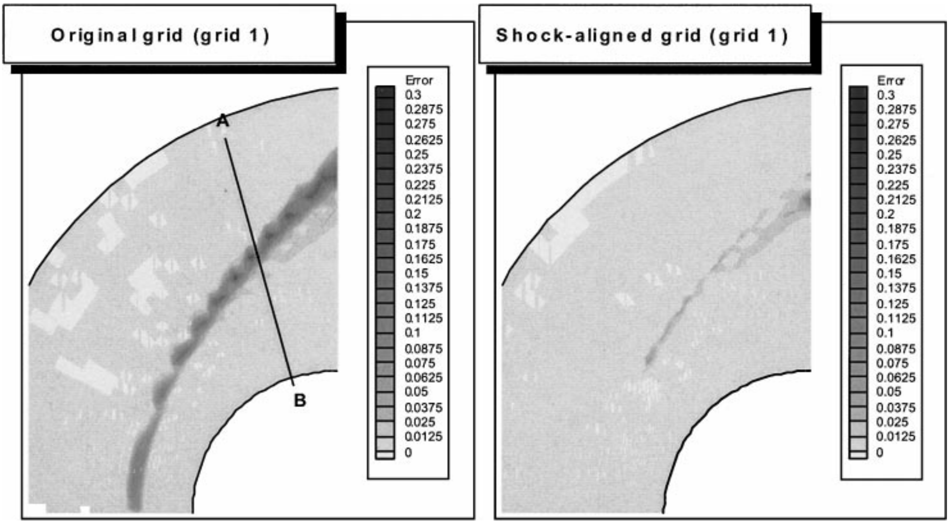

FIG. 8. Numerical error distributions.

3.4. Convergence Characteristics of SAGT

The convergence behavior of SAGT is checked at two steps as can be seen in Fig. 6: one at the sub-iteration step that determines shock position and the other at the whole-domain iteration step to examine the error by shocks in the whole computational domain. For complete SAGT results, more than two cycles are necessary. Since shock position in

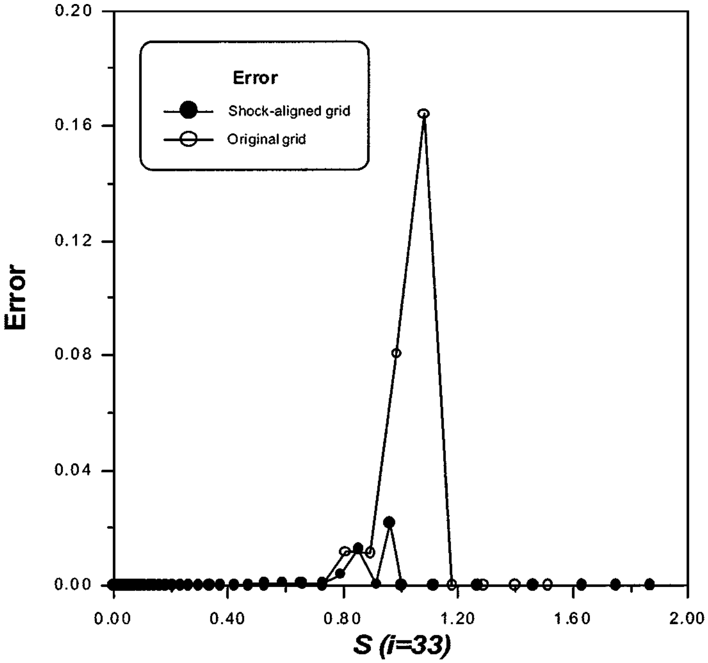

FIG. 9. Numerical errors along the line AB.

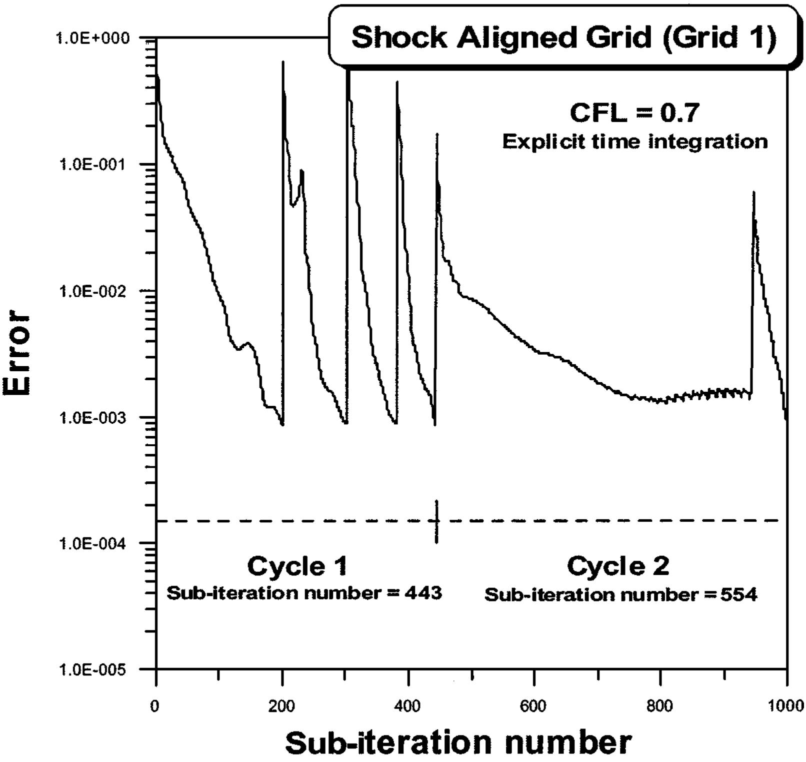

FIG. 10. Error history in each sub-iteration.

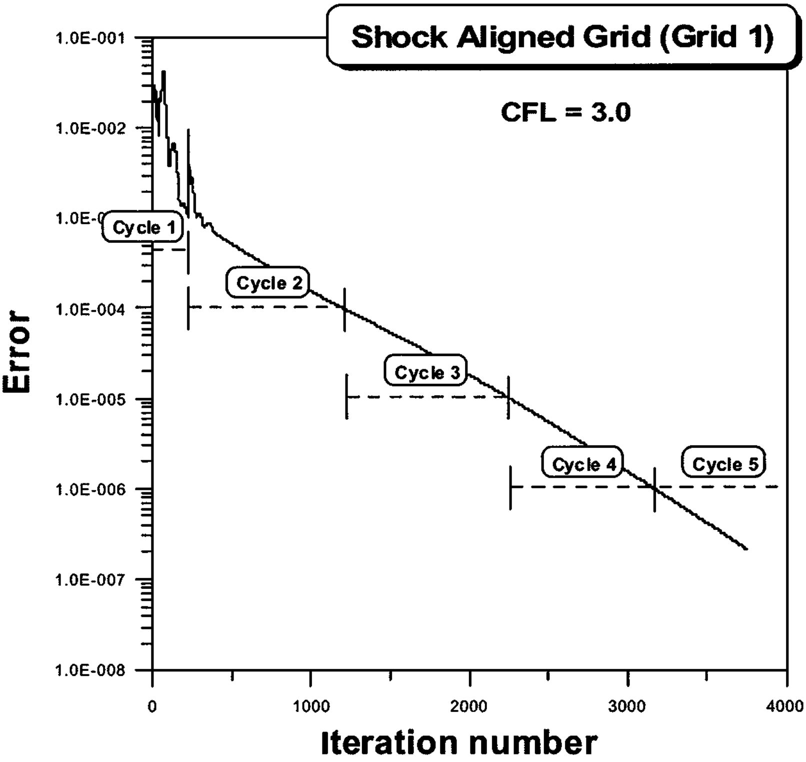

FIG. 11. Error history in whole-domain iterations of each cycle.

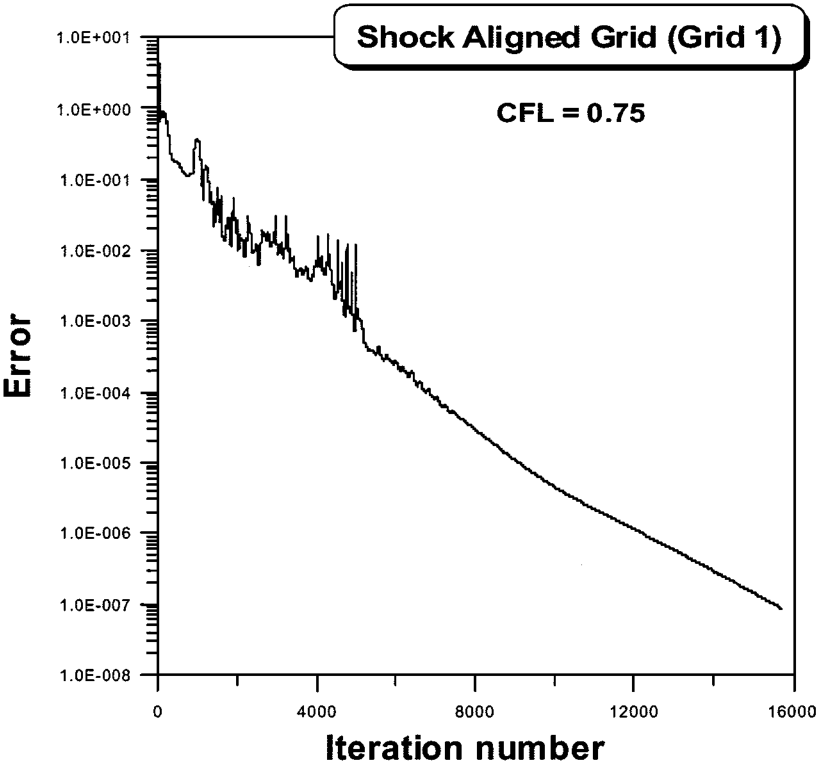

FIG. 12. Error history of the original grids.

the subiteration step is calculated based on the initial converged solution that contains the error by shocks, the result after Cycle 1 may not be free from errors. Figures 10 to 12 show the typical convergence behavior of SAGT with grid type 1 in Section 4.1. Figure 10 shows the error history for each sub-iteration. In Cycle 1, four sub-iterations are carried out, and two sub-iterations are carried out in Cycle 2. In calculating strong shocks, it is occasionally seen that solutions cannot be converged because of high frequency errors, as shown in sub-iterations of Cycle 2. The problematic region is commonly where the maximum error occurs in the computational domain. The error can be eliminated by the minute readjustment of grid points within the constraint of the threshold limits ($dp_{\min}$ and $dp_{\max}$), and convergence can be guaranteed. If the solution is not converged in previous the sub-iteration, the pressure behind the shock in the problematic region is calculated again as

$$p_{bs} = \frac{(p_{j+n} + dp_{\min} \cdot p_{fs})}{1 + dp_{\min}}, \quad n = 0, i_m - 2 < i < i_m + 2, \tag{38}$$

where i_m is the i-index where maximum error occurs in the previous sub-iteration.

Figure 11 shows the error history of the whole-domain iteration at each cycle. Although the CFL number is restricted by 0.75 in the original grids, it can increase up to 3 in shock-aligned grids since the error or instability by shocks is substantially reduced. It is noted that the location of grid points does not change after Cycle 2 since all pressure distributions satisfy the constraint of the threshold limits ($dp_{\min}$ and $dp_{\max}$) in the whole domain.

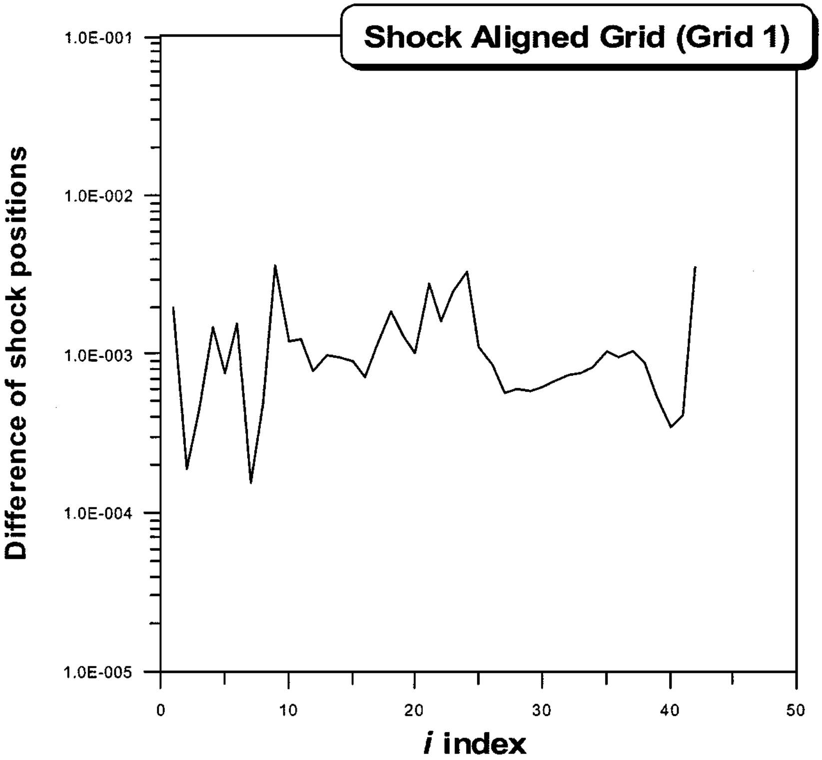

FIG. 13. Difference of shock position between Cycle 1 and Cycle 2 along *i*-index.

Figure 13 shows a delicate difference in shock position after Cycle 1 and Cycle 2, which is due to the error contained in the initial converged solution for Cycle 1. Table I shows the comparison of computational cost for SAGT with that of the original grids. Solutions are converged to an error level of 10^{-6}. Four cycles are executed for the complete implementation of SAGT. The extra computational cost is about 28% compared to the original grids. The time needed to perform sub-iterations in Cycles 1 and 2 takes only about 3% out of the total cost. The total cost is closely related to grid quality. As initial grid quality gets better, SAGT can be implemented much more efficiently. For example, if a high quality grid is presented initially as in Fig. 14, the computational burden of SAGT is negligible.

TABLE I

Comparison of Computational Cost

	Time (s)	Time/Time$_{\text{Original}}$ (%)
Original Grid	3647	100.00
SAGT		
Sub-iteration (Cycle 1)	22	0.60
Whole-domain iteration (Cycle 1)	68	1.86
Sub-iteration (Cycle 2)	28	0.76
Whole-domain iteration (Cycle 2)	313	8.58
Total time (Cycles 1–4)	1022	28.02

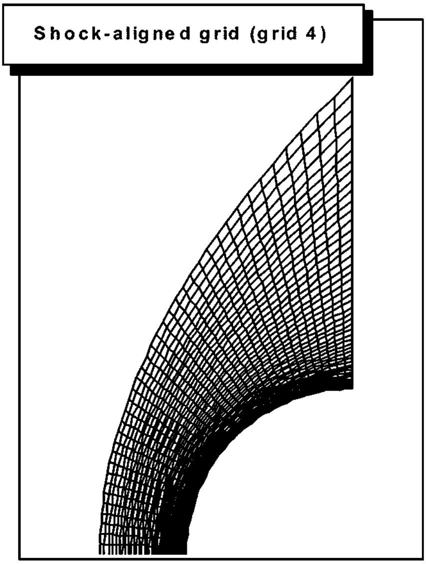

FIG. 14. Shock-aligned grid system.

4. NUMERICAL RESULTS FOR SAGT WITH AUSMPW+

In this section, we present the computed results of SAGT combined with the AUSMPW+ scheme. Test cases cover from calorically perfect gas flows to equilibrium and nonequilibrium gas flows.

4.1. Hypersonic Flows over a Blunt Body

The free stream conditions are

- calorically perfect gas,
- $M_\infty = 16.32$,
- $p_\infty = 82.95\ \text{N/m}^2$,
- $\rho_\infty = 5.557 \times 10^{-3}\ \text{kg/m}^3$,
- $\mu_\infty = 3.369 \times 10^{-6}\ \text{kg/m·s}^2$,
- $T_\infty = 52\ \text{K}$,
- $T_{wall} = 294.4\ \text{K}$,
- $Re = 1.4972 \times 10^5$,
- $Pr = 0.72$.

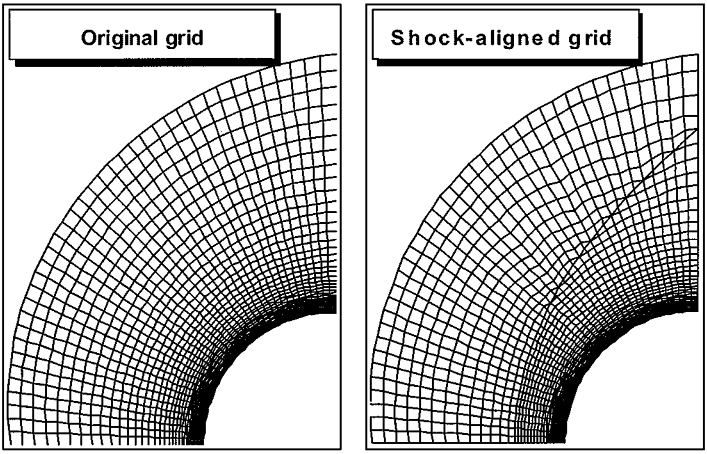

FIG. 15. Comparison of shock-aligned grids and original grids.

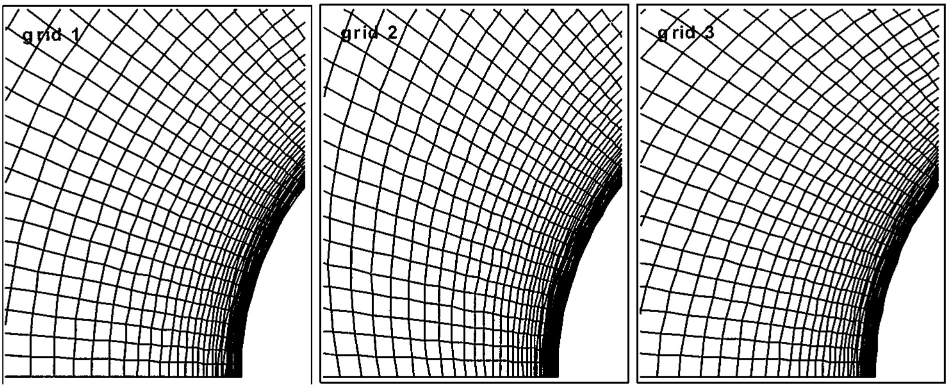

FIG. 16. Various grid types around a blunt body.

The conditions for the computation are

• Time integration:	CFL = 0.75, AF-ADI,
• Spatial discretization:	AUSMPW+, 3rd-order MUSCL with minmod limiter, the number of grid point = 40 × 60 (see Fig. 15),
• Boundary condition:	constant temperature wall,
• Threshold values:	$dp_{\max} = 0.05$ and $dp_{\min} = 0.01$.

As a standard test case that examines the effects of a strong shock wave and a large gradient in a boundary layer, a hypersonic blunt body problem is chosen. The primary concern is to handle the error due to computational grid and numerical instability. In the original grids, the time step due to the CFL condition is severely restricted because of the instability induced from a stiff gradient near a shock. Thus the CFL number cannot be greater than 0.75. SAGT, however, relaxes the restriction substantially and the CFL number can be increased to 3.0. The other advantage, which is more important, is that accurate aerodynamic coefficients can be obtained almost irrespective of initial grid distribution.

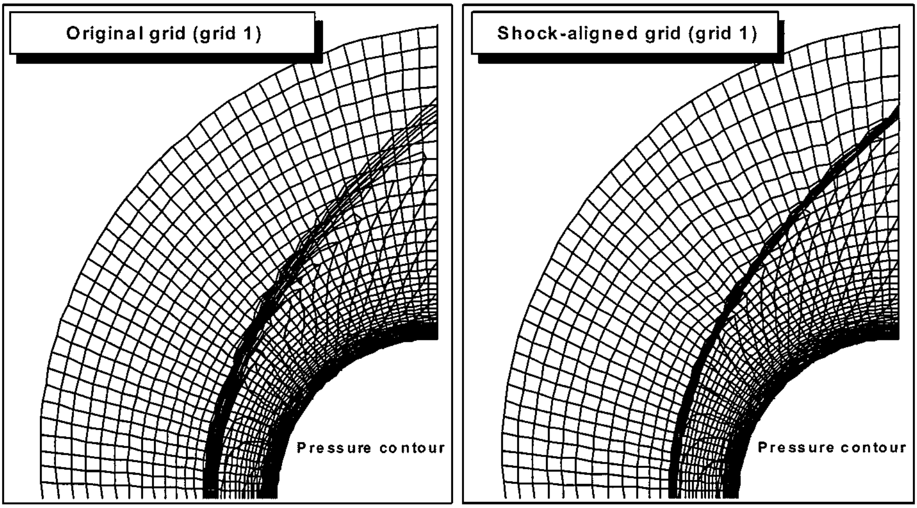

FIG. 17. Comparison of pressure distributions.

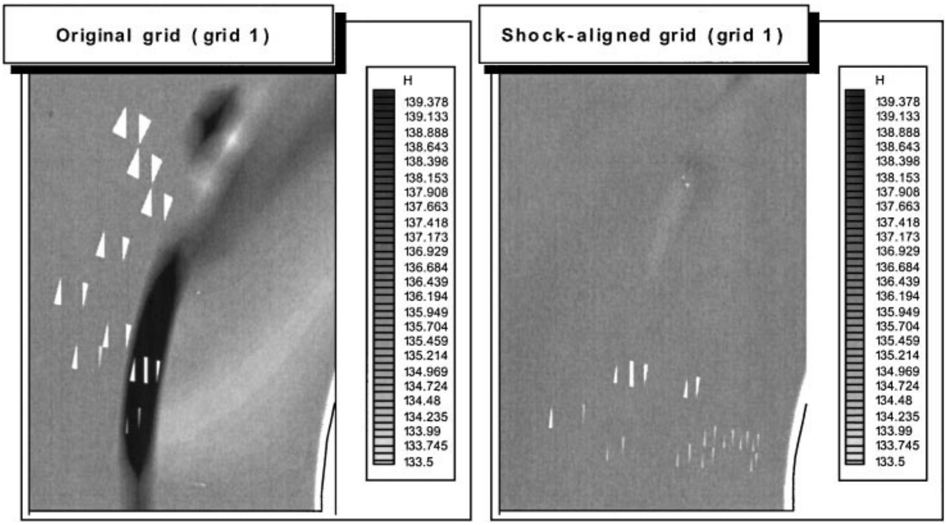

FIG. 18. Comparison of total enthalpy for grid type 1.

Figure 16 shows three types of grids around the blunt body depending on the grid quality around the stagnation streamline: grid type 1 is normal to the stagnation streamline, grid type 2 is greater than a 90 degree angle, and grid type 3 is smaller than a 90 degree angle. Figures 17, 19, and 21 show that shocks are captured very crisply in shock-aligned grid systems and the resolution is independent of initial grid distribution. In non-shock-aligned grids, however, shocks are diffused over a few cells and influenced by an initial system. Thus, the error intrinsically exists in converged solutions. Figures 18, 20, and 22 show the total enthalpy error induced by the steady shock and its propagation on the downstream side in each grid system. Figures 23 and 24 confirm that the surface heating rate is indeed highly affected by a grid system, and the error from the shock actually influences the flow physics at the wall. In grid type 2 the solution yields a higher total enthalpy in the stagnation

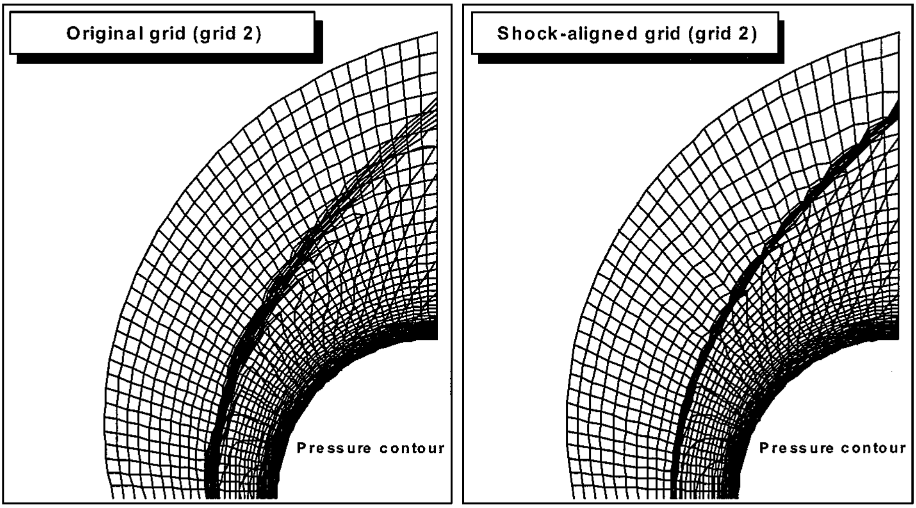

FIG. 19. Comparison of pressure distributions.

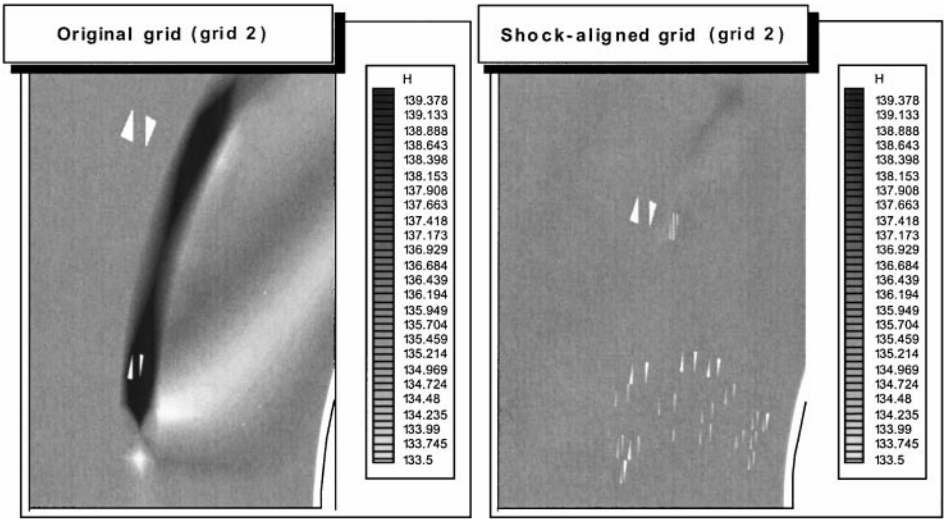

FIG. 20. Comparison of total enthalpy for grid type 2.

region and the surface heating rate is overestimated. The opposite behavior can be observed from the solution with grid type 3. In contrast, in shock-aligned grids, the total enthalpy is preserved and the influence of grid distribution is eliminated. Mathematically, the type of the governing equations in the stagnation region becomes amorphous because the convection velocity approaches zero. Thus the order of error can be easily larger than a convection term, and a little numerical error may influence the solution significantly, especially for sensitive aerodynamic coefficients such as the surface heating rate.

Vorticity is also very sensitive to the error since it is the derivative of basic flow variables. The relation between vorticity and the error in the shock region was investigated in detail by Lee and Zhong using accurate shock-capturing methods such as TVD and ENO schemes [1]. Aside from the accuracy issue of shock-capturing schemes in non-shock-aligned grids, they

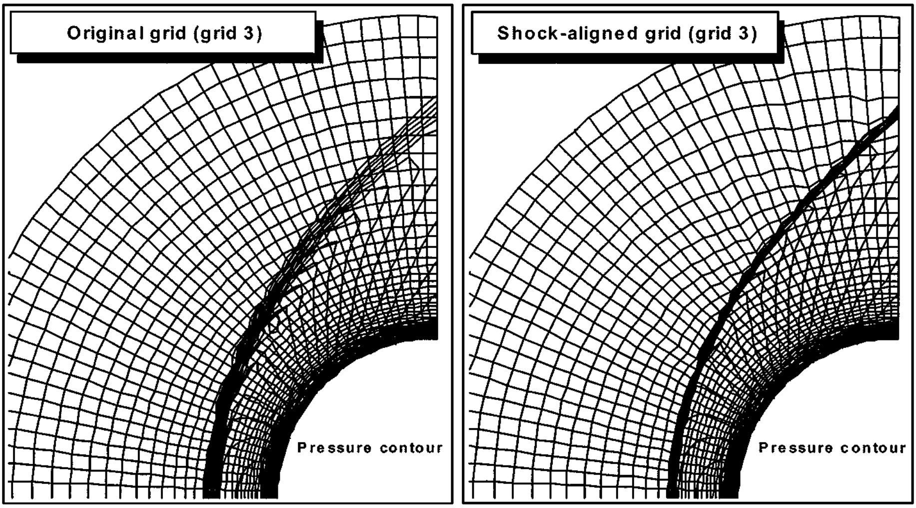

FIG. 21. Comparison of pressure distributions.

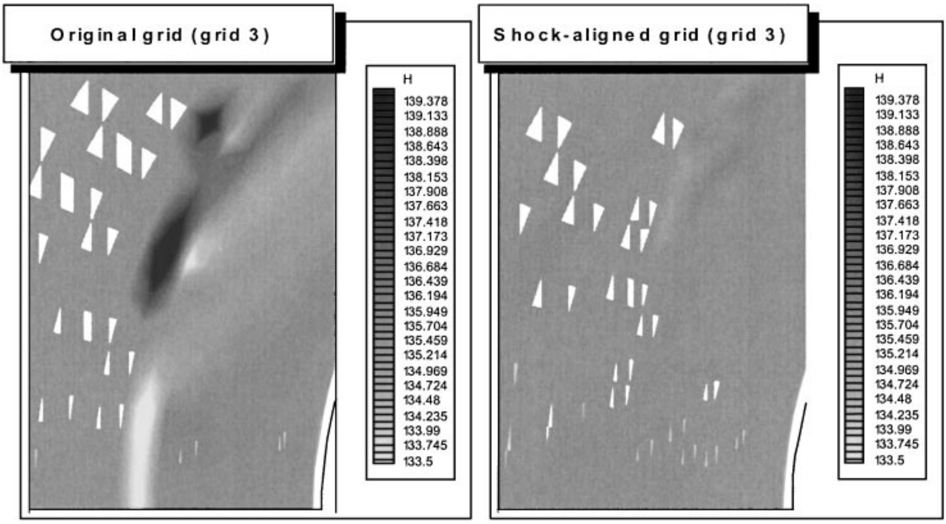

FIG. 22. Comparison of total enthalpy for grid type 3.

also observed that grid resolution and grid alignment seriously influence the production of spurious post-shock oscillations. It was shown that grid refinement reduced the wavelength of spurious oscillations but did not affect the amplitude significantly. Grid alignment, on the other hand, substantially decreased the amplitude of spurious oscillations but did not eliminate it completely. As a remedy, to remove the vorticity oscillations completely, a shock-fitting technique was adopted. In the present work, we advocate the shock-capturing approach because of its broad applicability, and we try to cure this problem by using a

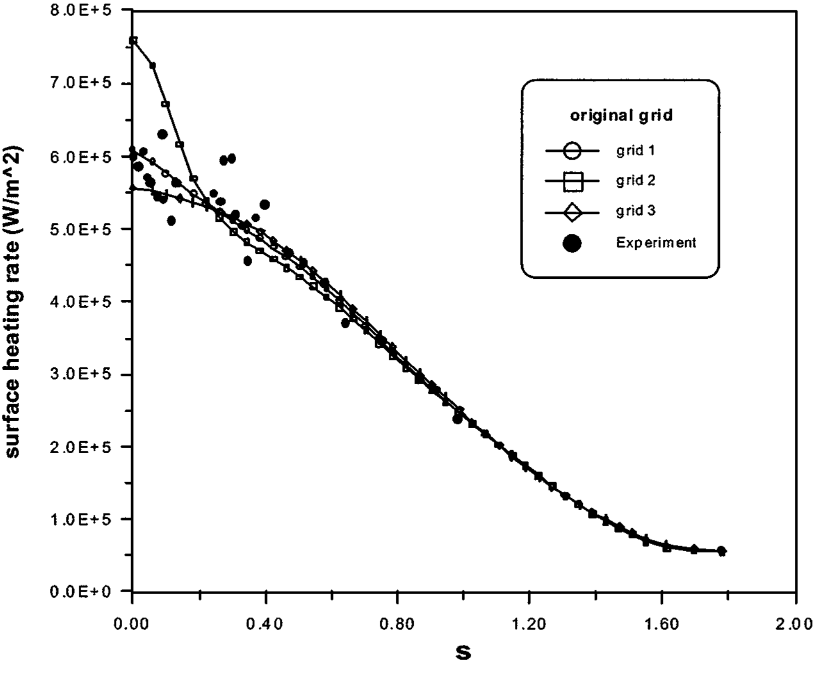

FIG. 23. Comparison of surface heating rates for the original grid systems.

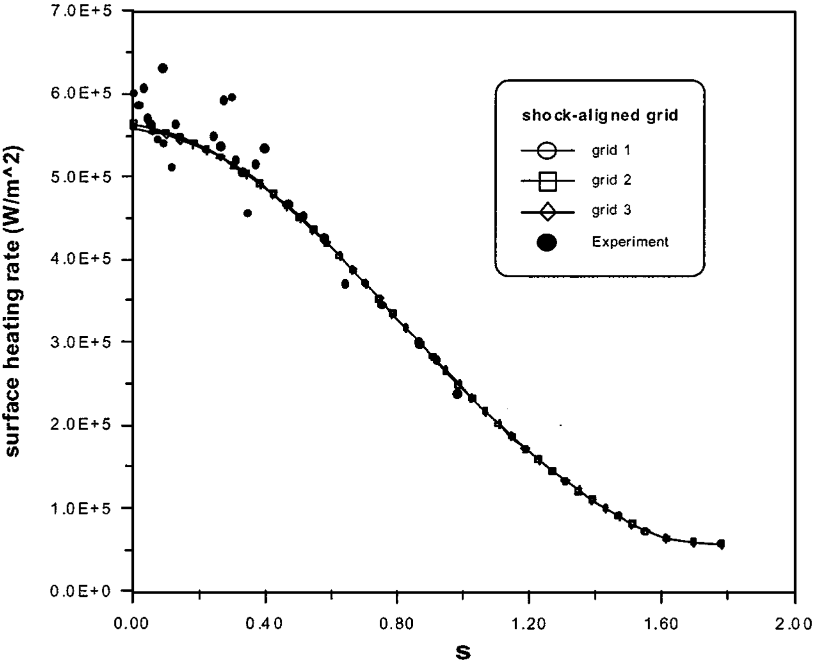

FIG. 24. Comparison of surface heating rates for shock-aligned grid systems.

SAGT with AUSMPW+. Vorticity is calculated as

$$\oiiint \omega \, dV = \oiiint \nabla \times \boldsymbol{V} \, dV = \oint \boldsymbol{V} \cdot d\boldsymbol{s} \tag{39}$$

$$\omega = \frac{1}{V}\left(\int v \, dx + \int u \, dy \right), \tag{40}$$

where ω is vorticity, $\boldsymbol{V}$ is the velocity vector, and V is a cell volume. Figure 25 shows

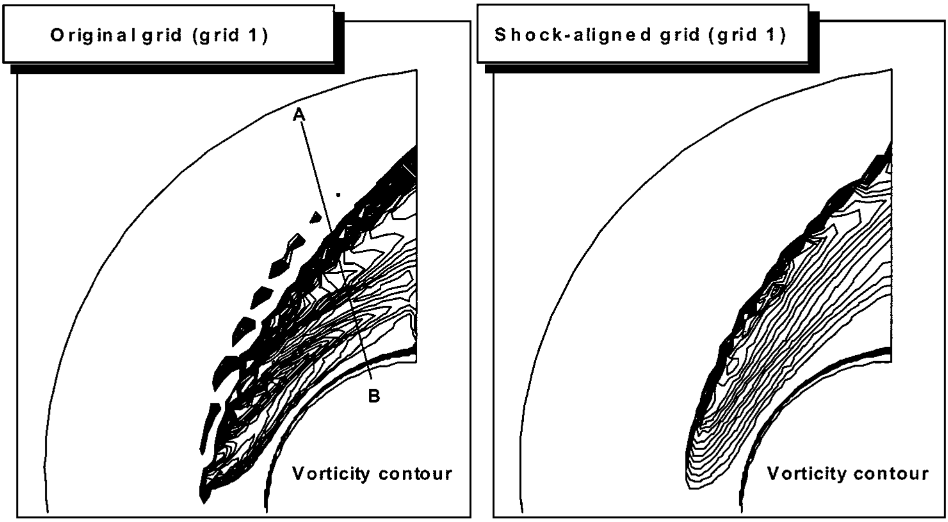

FIG. 25. Comparison of vorticity contours.

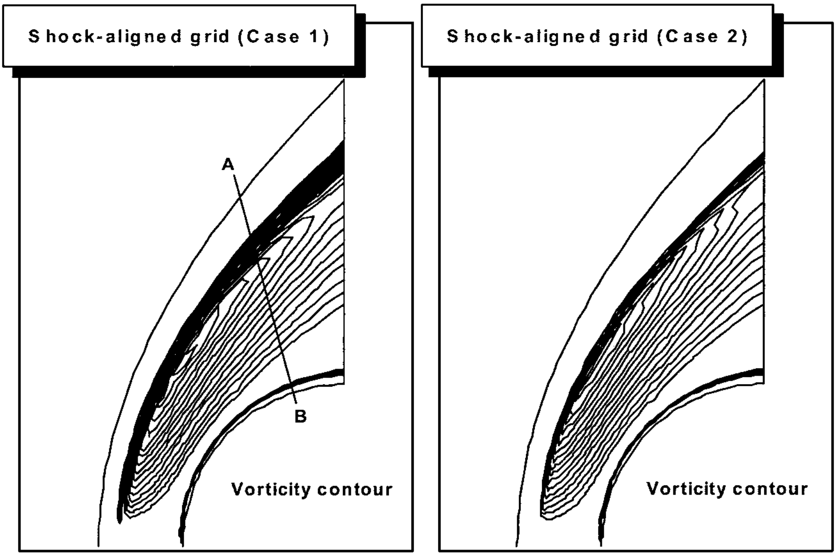

FIG. 26. Comparison of vorticity contours.

the vorticity contours with 50 contour levels in the original grids (grid 1). As shown in Fig. 27, they are highly oscillatory in the original grids while SAGT provides a remarkable improvement. Even with SAGT, however, the result is not shown to be perfect. It is due to the error induced at kinked grids of an initial grid system. Although the error is substantially reduced in shock-aligned grids as shown in Fig. 9, a little remnant produces a noticeable vorticity oscillation. Figures 26 and 28 show the results in a shock-aligned grid system with different formulations for the numerical speed of sound. As can be seen in Fig. 14, the final shock-aligned grids do not contain the change of grid connectivity since the quality of the initial grids is good. The averaged speed of sound of $c_s = (c_L + c_R)/2$ is used for Case 1, and the newly defined speed of sound (Eq. (13)) is used for Case 2. As a result, Case 1 cannot support the capturing of an oblique shock in one cell interface. As can be seen in Fig. 28, the choice of the speed of sound critically influences the vorticity distribution. In Case 1, vorticity exhibits an oscillatory behavior in the shock region even in a shock-aligned grid system because the numerical scheme adopted cannot capture a shock without numerical error. Therefore, an accurate numerical scheme and grid reconstruction scheme should be combined appropriately in order to treat this problem within the framework of a shock-capturing method.

4.2. Reflection and Intersection of Shock Waves

The free stream conditions are

- calorically perfect gas,
- $M_\infty = 3.0$,
- wedge angle = 5°.

The conditions for the computation are

- Time integration: CFL = 0.5, AF-ADI,
- Spatial discretization: AUSMPW+, 3rd-order MUSCL with Minmod limiter, the number of grid point = 50 × 30, 50 × 45 (see Figs. 29 and 32),

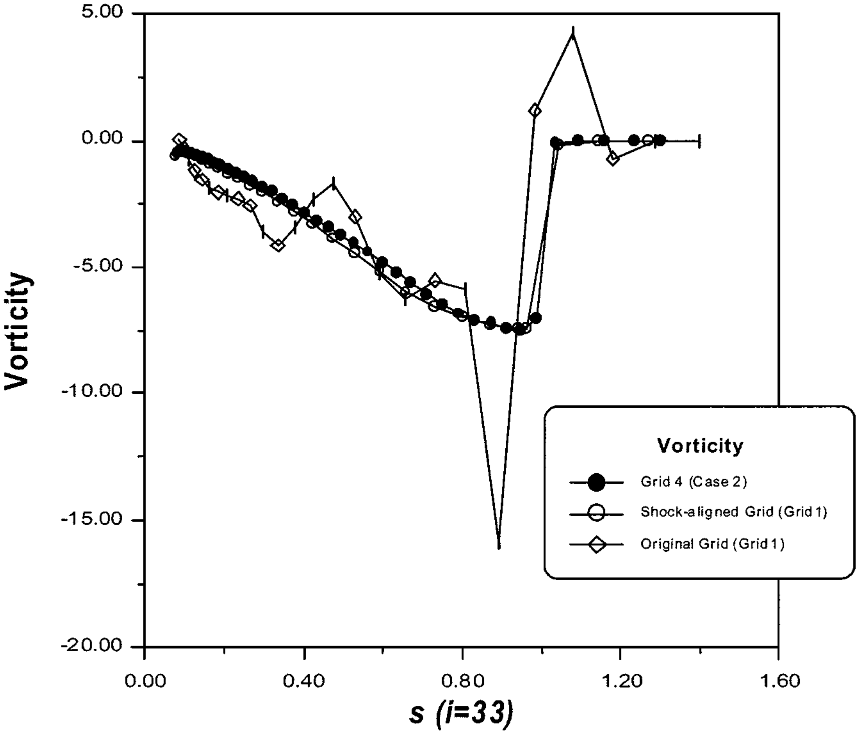

FIG. 27. Comparison of vorticity distributions in Grid 1 along line AB.

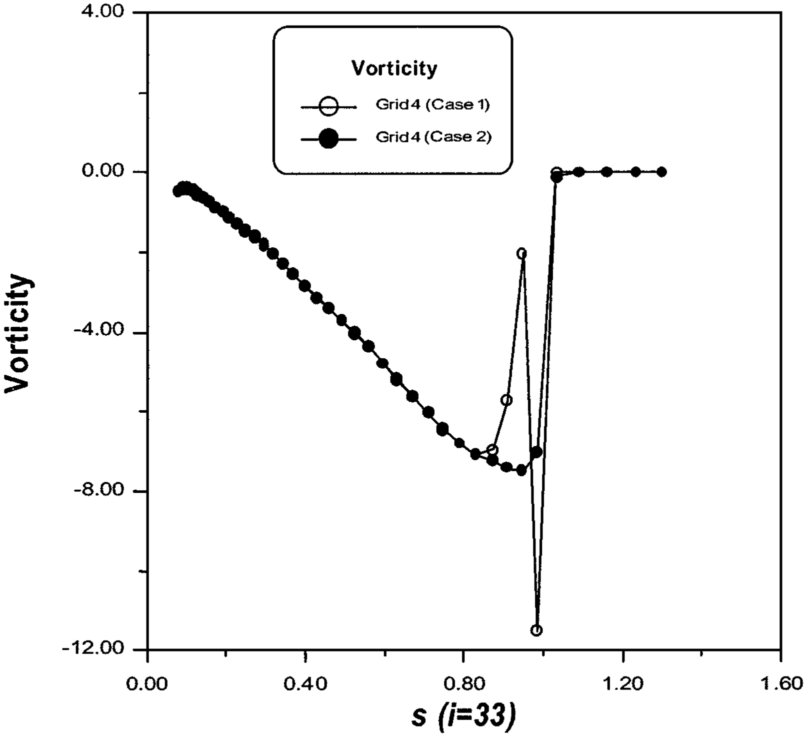

FIG. 28. Comparison of vorticity distributions in shock-aligned grid system along line AB.

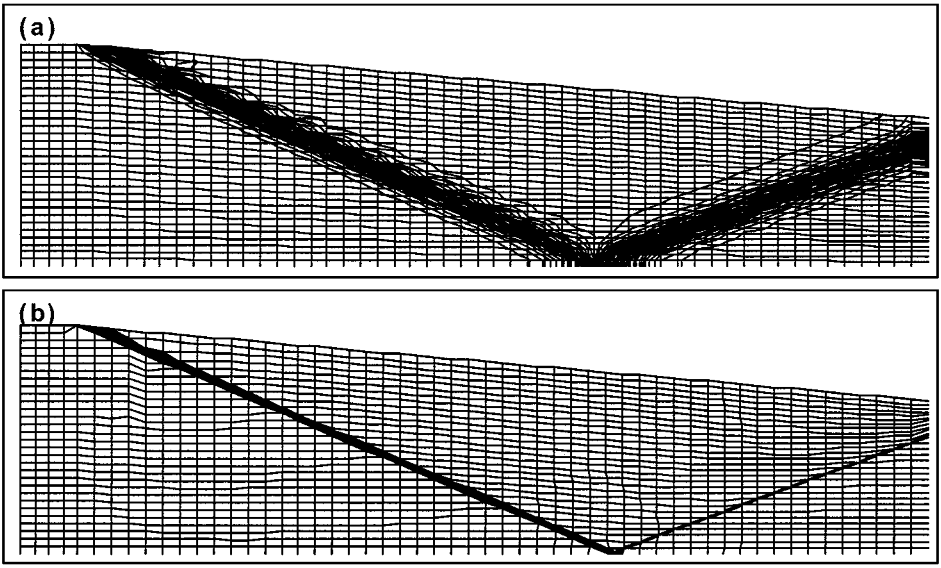

FIG. 29. Comparison of pressure distributions.

- Boundary condition: slip condition,
- Threshold values: $dp_{\max} = 0.01$ and $dp_{\min} = 0.005$.

In order to examine the flexibility and robustness of SAGT, the reflection and intersection of shocks are investigated. These test problems are quite important since shock intersection

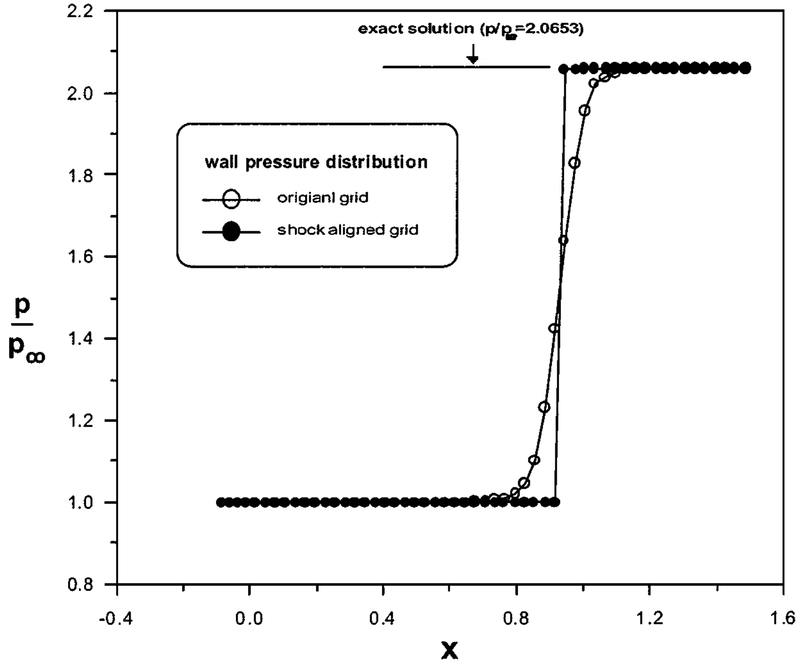

FIG. 30. Comparison of wall pressure distributions.

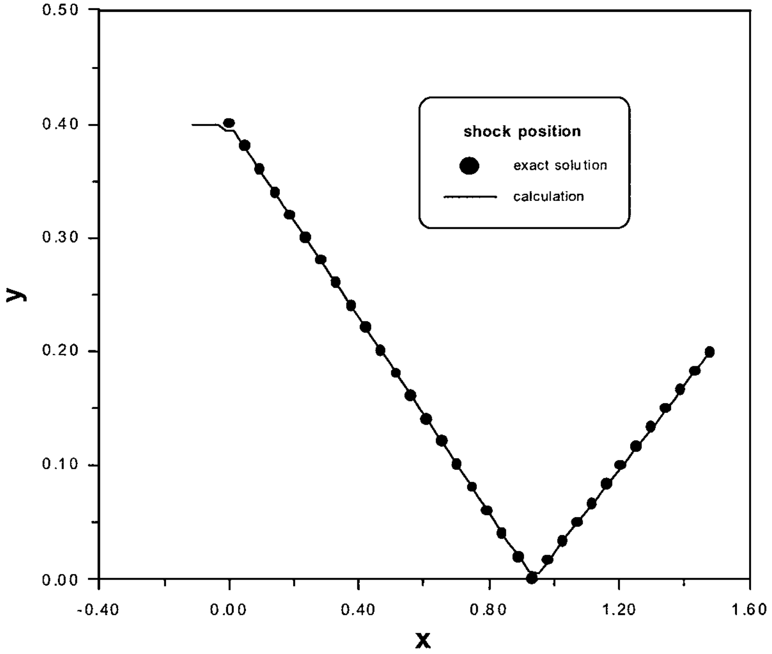

FIG. 31. Comparison of shock position for shock reflection problem.

and reflection are very basic phenomena in the analysis of complex flow problems. As can be seen in Figs. 29 and 30, the oblique shock is captured through eight cell interfaces in the original grids, while it is captured over only one cell interface in shock-aligned grids. Figures 30 and 31 confirm that the calculated shock position is identical to the exact solution. In case of shock intersection, similar performance can be observed from the results of Figs. 33 to 35. This example supports the fact that SAGT can be applied to flows involving complex shock interaction.

4.3. Equilibrium and Nonequilibrium Flows around a Cylinder

The free stream conditions are

- equilibrium and nonequilibrium gas,
- $M_\infty = 15$,
- $p_\infty = 663.41\ \mathrm{N/m^2}$,
- $\rho_\infty = 9.8874 \times 10^{-3}\ \mathrm{kg/m^3}$,
- $\mu_\infty = 1.514 \times 10^{-5}\ \mathrm{kg/m \cdot s^2}$,
- $T_\infty = 233.75\ \mathrm{K}$,
- $T_{wall} = 1168.7\ \mathrm{K}$,
- $Re = 2.0 \times 10^5$.

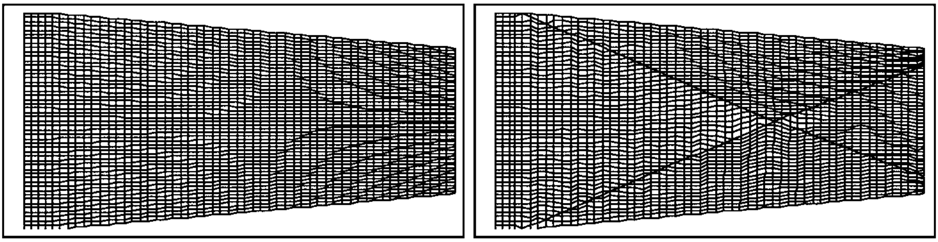

FIG. 32. Grid systems for shock intersection problem.

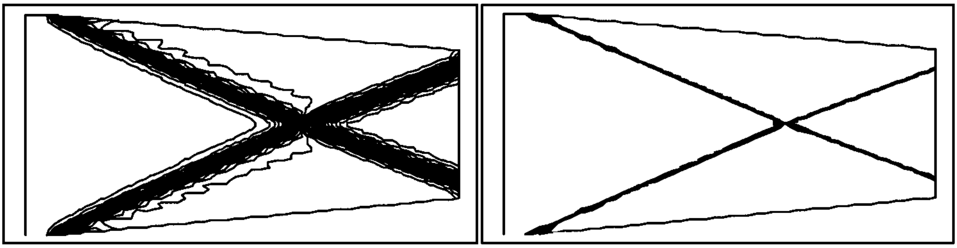

FIG. 33. Comparison of pressure distributions for shock intersection problem.

The conditions for the computation are

- Time integration: CFL = 0.5, LU-SGS,
- Spatial discretization: AUSMPW+, 3rd-order MUSCL with minmod limiter, the number of grid point = 80×55 (see Fig. 36),
- Boundary condition: constant temperature wall (fully catalytic wall),
- Threshold values: $dp_{\max} = 0.05$ and $dp_{\min} = 0.01$.

Figure 36 is the result of SAGT applied to equilibrium and nonequilibrium flows and shows high resolution in capturing the bow shock. The robustness of SAGT can be observed again in Fig. 37. It is difficult to compare shock positions of the two-temperature model with those of the four-temperature model because of the delicate difference. However, by applying SAGT, the minute difference of shock positions could be obtained directly. Even though the source term of the governing equations in nonequilibrium gas produces the broad area of shock transition, it is observed that SAGT is still available in the highly nonequilibrium region.

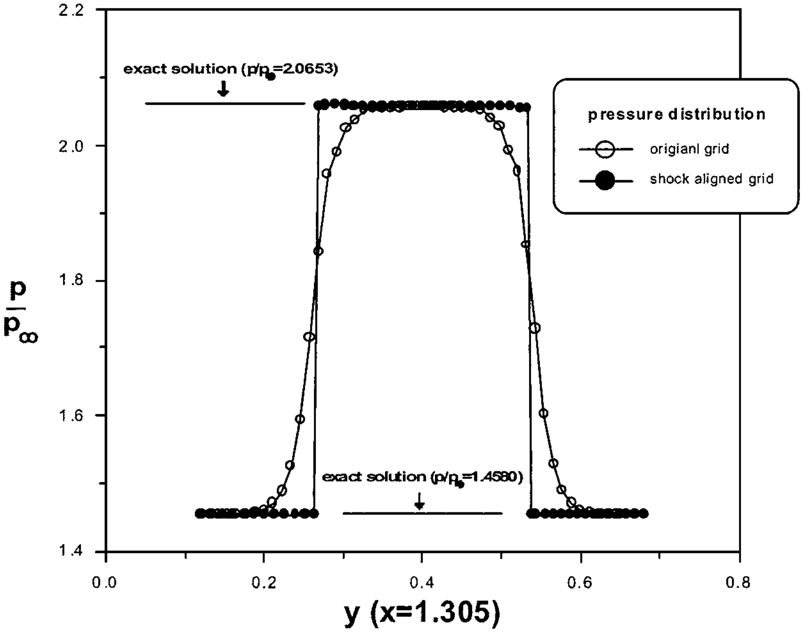

FIG. 34. Pressure distributions at $x = 1.305$.

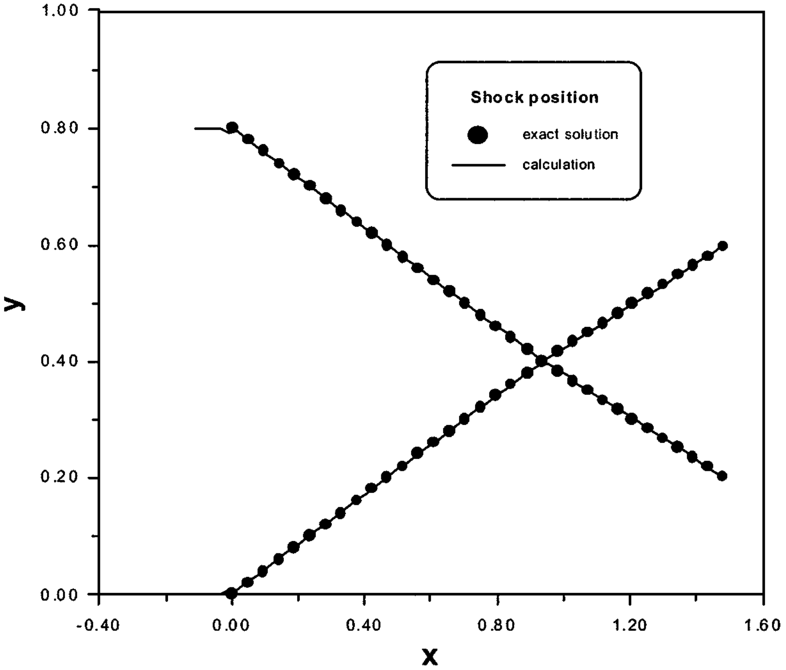

FIG. 35. Comparison of shock position for shock intersection problem.

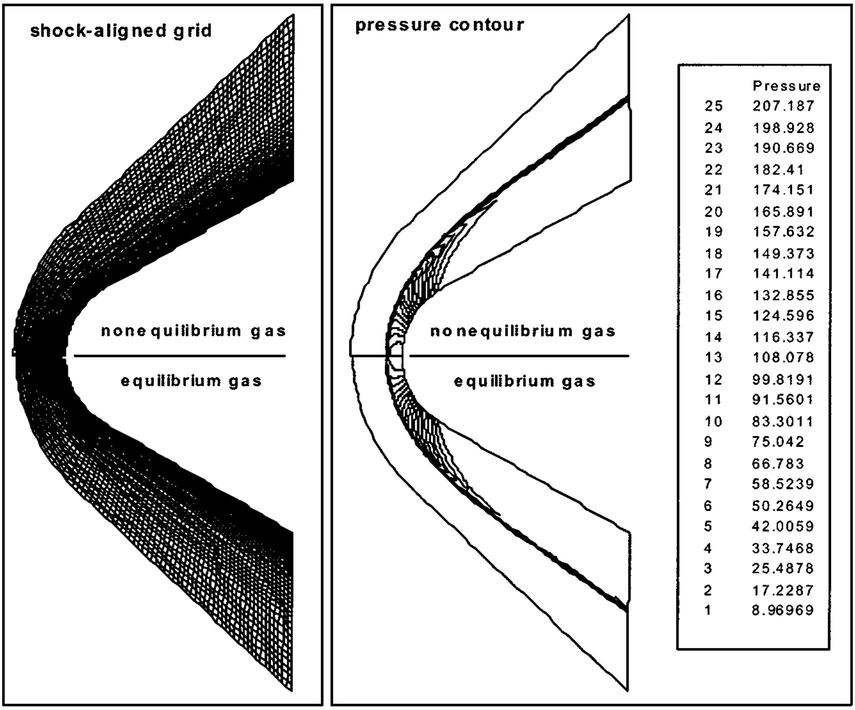

FIG. 36. Grid system and pressure distributions around a blunt cone.

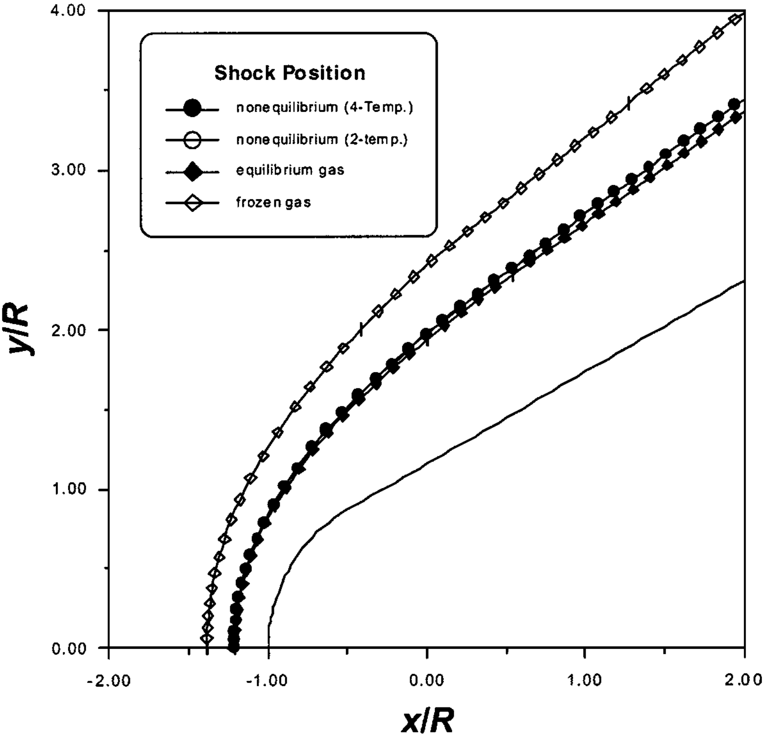

FIG. 37. Comparison of shock positions for various gas models.

4.4. Nonequilibrium Flow around a Blunt Cone

This test case is for the comparison of a computed shock position with the experimental data in the ballistic range. The free stream conditions are

- nonequilibrium gas,
- $u_\infty = 3.63$ km/s,
- $p_\infty = 2400$ N/m^2,
- $T_\infty = 293$ K,
- $R = 0.007$ m,
- axisymmetric flow.

The conditions for the computation are

• Time integration:	CFL = 0.5, LU-SGS,
• Spatial discretization:	AUSMPW+, 3rd-order MUSCL with minmod limiter, the number of grid point = 150 × 40,
• Boundary condition:	slip condition,
• Threshold values:	$dp_{\max} = 0.05$ and $dp_{\min} = 0.01$.

Figures 38 and 39 show the standing shock distance computed by SAGT with AUSMPW+, which agrees very well with experimental data. Again, the oblique shock is not diffused and captured over only one cell interface. This confirms again the accuracy of the numerical solution based on SAGT and the speed of sound of Eqs. (12) and (13).

4.5. Nonequilibrium Flow around a Double Cone

This test case involves the phenomenon of shock intersection and reflection of expansion fan in a nonequilibrium gas. The free stream conditions are

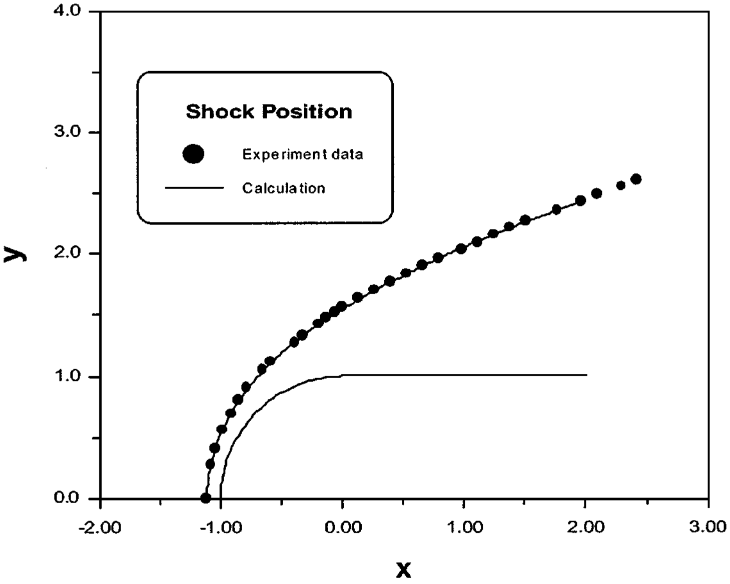

FIG. 38. Comparison of shock distance with experimental data.

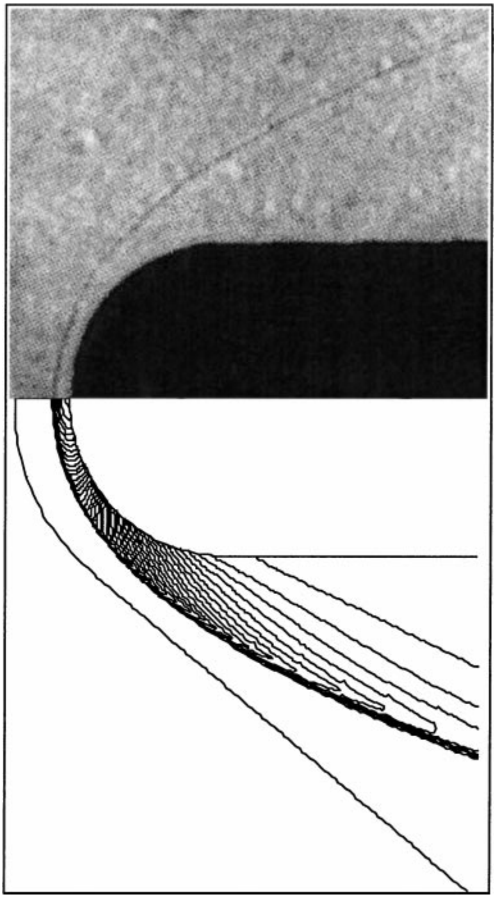

FIG. 39. Comparison between computed result and experiment.

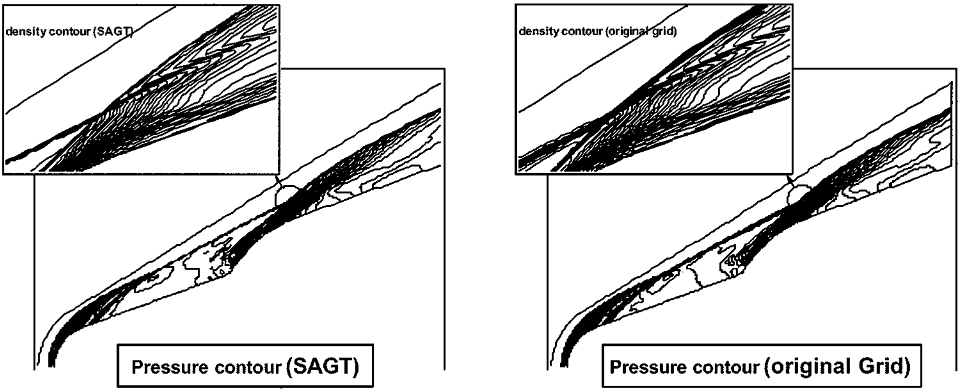

FIG. 40. Pressure and density distributions around a double cone.

- nonequilibrium gas,
- $\rho_\infty = 9.8874 \times 10^{-3}$ kg/m^3,
- $T_{wall} = 1168.7$ K,
- $M_\infty = 15$,
- $\mu_\infty = 1.514 \times 10^{-5}$ kg/m $\cdot$ s^2,
- $Re = 2.0 \times 10^5$,
- $p_\infty = 663.41$ N/m^2,
- $T_\infty = 233.75$ K,
- axisymmetric flow.

The conditions for the computation are as follows:

- Time integration: CFL = 0.5, LU-SGS,
- Spatial discretization: AUSMPW+, 3rd-order MUSCL with minmod limiter, the number of grid point = 150 × 60,
- Boundary condition: constant temperature wall (fully catalytic wall),
- Threshold values: $dp_{\max} = 0.05$ and $dp_{\min} = 0.01$.

The comparison of complex flow structure is shown in Fig. 40. By removing the numerical error near the shock intersection region, the shear layer developing from the intersection point is computed more accurately. Although SAGT can be applied to various shock interaction problems, it might have a limited applicability in problems with very complex physical phenomena compared to the number of grid points. For example, in the region where a shock and expansion fan coexist very closely, such as for separation bubbles caused by shock/boundary interaction, it is difficult to judge the shock range in a coarse grid system (Steps 1.a and 1.b in Section 3.2.1). As a result, the shock position may not be easily converged. Of course, if grid points are numerous enough, there is no difficulty.

4.6. Equilibrium Shock Wave/Shock Wave Interaction (Type IV)

The free stream conditions are

- equilibrium gas,
- $\rho_\infty = 5.4656 \times 10^{-3}$ kg/m^3,
- $Re = 1.45 \times 10^5$,
- $M_\infty = 16.33$,
- $T_\infty = 52.27$ K,
- impinging shock angle = 13°.
- $p_\infty = 88.003$ N/m^2,
- $T_{wall} = 294.44$ K,

The conditions for the computation are

- Time integration: CFL = 0.5, AF-ADI,
- Spatial discretization: AUSMPW+, the number of grid point = 161 × 65,

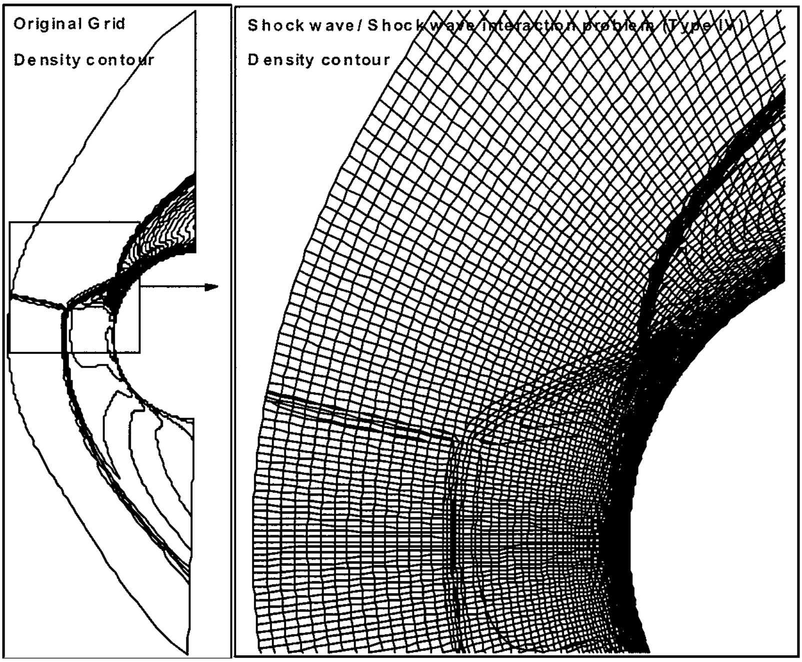

FIG. 41. Density distribution of shock/shock interaction (Type IV) in the original grid system.

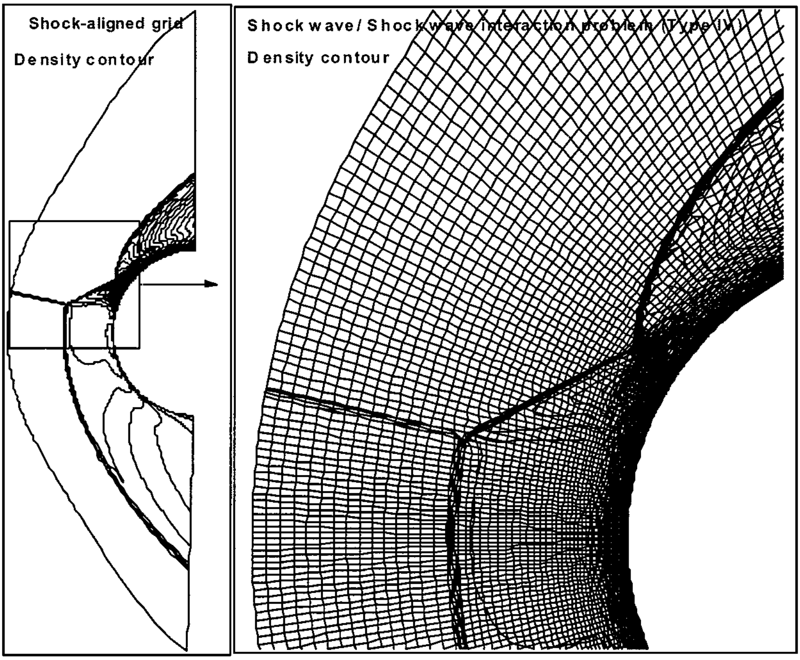

FIG. 42. Density distribution of shock/shock interaction (Type IV) in the shock-aligned grid system.

- Boundary condition: constant temperature wall,
- Threshold values: $dp_{\max} = 0.1$ and $dp_{\min} = 0.01$.

Flow conditions are the same as in Ref. [6]. Type IV shock/shock interaction phenomena are observed when a shock is impinging on a subsonic region behind a bow shock. This type of interaction has been shown to be inherently unsteady in perfect gas flows [7]. Even in equilibrium gas flows, a fully steady case has not been reported yet. Although SAGT is essentially for steady problems, it can be applied to this case successfully since the flow unsteadiness is relatively weak. Owing to unsteady shock motion, $dp_{\max}$ is chosen to 0.1. Figures 41 and 42 show more closely the results of SAGT for the complex shock structure, especially the transmitted shock. These results also suggest that SAGT can be extended to fully unsteady problems with further improvement by newly defining the speed of sound at a cell interface.

5. CONCLUSIONS

As an accurate, robust, and efficient grid reconstruction scheme to compute hypersonic flows, the SAGT (shock-aligned grid technique) is proposed. SAGT is a method to reconstruct a grid system *automatically*, which supports the capturing of a shock with minimal numerical error. With the advantage of the AUSMPW+ scheme that is able to capture normal or oblique shocks through only one cell interface in shock-aligned grids, SAGT provides a very accurate shock resolution and a solution that is not influenced by initial grid distribution. Also, the time step limit resulting from the CFL condition is considerably relieved by removing the shock-induced error in non-shock-aligned grids. Aerodynamic coefficients or higher order derivative terms that are highly sensitive to a little numerical error, such as surface heating rate or vorticity, can also be accurately calculated without unphysical oscillations. These advantages are thought to be important in computing problems involving strong shocks or physical oscillations. Numerous computed results confirm that SAGT is robust enough to be applied in equilibrium and nonequilibrium flows.

ACKNOWLEDGMENTS

This research was supported in part by a grant from the BK-21 Program for Mechanical and Aerospace Engineering Research at Seoul National University and a grant from the Korea Science and Engineering Foundation (Grant 98-0200-14–01-3). The authors appreciate the referees for their careful and rigorous comments on this manuscript.

REFERENCES

1. T. K. Lee and X. Zhong, Spurious numerical oscillations in simulation of supersonic flows using shock-capturing schemes, *AIAA J.* **37**(3), 313 (1999).
2. S. Srinivasan, J. C. Tannehill, and K. J. Weilmuenster, *Simplified Curve Fits for the Thermodynamic Properties of Equilibrium Air*, NASA RP-1181 (Aug. 1987).
3. R. N. Gupta, K. P. Lee, R. A. Thompson, and J. M. Yos, *Calculations and Curve Fits of Thermodynamic and Transport Properties for Equilibrium Air to 30000 K*, NASA RP-1260 (1991).
4. T. K. S. Murthy, *Computational Methods in Hypersonic Aerodynamics* (Kluwer Academic, Dordrecht, 1991).
5. C. Park, Review of chemical-kinetic problems of future NASA missions, I: Earth Entries, *J. Thermophys. Heat Transfer* **7**(3), 385 (1993).

6. R. K. Prabhu, J. R. Stewart, and R. R. Thareja, *Shock Interference Studies on a Circular Cylinder at Mach 16*, Technical Paper 90-0606 (AIAA Press, Washington, DC, 1990).
7. G. H. Furumoto and X. Zhong, *Numerical Simulation of Viscous Unsteady Type IV Shock–Shock Interaction with Thermochemical Nonequilibrium*, Technical Paper 97-0982 (AIAA Press, Washington, DC, 1997).
8. K. H. Kim, C. Kim, and O. Rho, *Accurate Computations of Hypersonic Flows Using AUSMPW+ Scheme and Shock-Aligned Grid Technique*, Technical Paper 98-2442 (AIAA Press, Washington, DC, 1998).
9. K. H. Kim and O. H. Rho, An improvement of AUSM schemes by introducing the pressure-based weight functions, *Comput. Fluids* **27**(3), 311 (1998).
10. C. Hirsh, *Numerical Computation of Internal and External Flows*, Vols. 1, 2 (Wiley, New York, 1990).
11. H. C. Yee, G. H. Kolpfer, and J. L. Montague, *High-Resolution Shock Capturing Schemes for Inviscid and Viscous Hypersonic Flows*, NASA TM 101088 (1989).
12. J. V. Rosendale, *Floating Shock Fitting Via Lagrangian Adaptive Meshes*, Technical Paper 95-1721 (AIAA Press, Washington, DC, 1995).